

Oxidation Resistance of Additively Manufactured Inconel 718 for Gas Turbine Applications

by

Adria Barcelo Singh

A Thesis submitted to
the Faculty of Graduate Studies and Research
in partial fulfilment of the
requirements for the degree of
Master of Applied Science

Ottawa-Carleton Institute for
Mechanical and Aerospace Engineering

Department of Mechanical and Aerospace Engineering
Carleton University
Ottawa, Ontario, Canada
December 2019

Copyright ©

2019 – Adria Barcelo Singh

The undersigned recommend to
the Faculty of Graduate Studies and Research
acceptance of the Thesis

**Oxidation Resistance of Additively Manufactured Inconel 718 for
Gas Turbine Applications**

Submitted by **Adria Barcelo Singh**
in partial fulfilment of the requirements for the degree of
Master of Applied Science

X. Huang, Thesis Supervisor

R. Miller, Department Chair

Carleton University
2019

Abstract

This research investigates the oxidation behaviour of an additively manufactured (AM) superalloy Inconel 718 and compares its oxidation performance to that of wrought Inconel 718. A plasma arc additive manufacturing process was developed and utilized to manufacture the AM specimens. All specimens were subjected to exposures at 800°C and 900°C. The oxidized specimens were analysed using Scanning Electron Microscopy (SEM) and Energy Dispersive Spectroscopy (EDS). Both surface oxide and cross-section microstructure were examined, in addition to microstructure changes in the substrate. The results showed that the two alloys had similar weight changes over the periods of 50-400 hours at both temperatures. However, the microstructure changes on the surface and in the substrate were different. The thickness of the chromia oxide scale formed on AM Inconel 718 was consistently thinner than that on the wrought specimens. There was also more internal oxidation on the AM specimens, particularly after longer exposure at high temperature. In addition, the formation of a subscale Nb-rich layer was observed between outer chromia and substrate on all specimens, except on the AM specimens exposed to 800°C for 100 hours, this layer contributed to the integrity of the chromia oxide layer. Based on the preliminary results, it was concluded that the AM material, when exposed to 900°C, had slightly inferior oxidation performance than the wrought alloy, attributable a thicker and more stable chromia oxide layer and to less internal oxidation.

Acknowledgements

I would like to thank Carleton University and the Department of Mechanical Engineering for giving me the opportunity to perform this research I want to thank my advisor, Dr. Xiao Huang, for her support, insight, patience and encouragement during this process.

I would like to thank all of my friends and family members for their continued support and cheering me on when things were tough.

I would like to thank my parents, Mario and Roxana, and my fiancé Eduardo for being a constant source of love and encouragement, and never letting me give up.

Lastly, to my dear sister. You are awesome and you are the best.

Thank you.

Table of Contents

Abstract.....	iii
Acknowledgements.....	iv
Table of Contents.....	v
List of Tables.....	vii
List of Figures.....	ix
Nomenclature.....	xiii
Chapter 1: Introduction.....	1
1.1 Preamble.....	1
1.2 Objective.....	3
1.3 Thesis structure overview.....	3
Chapter 2: Literature Review.....	5
2.1 Gas turbines and operating environments.....	5
2.2 Nickel and Nickel-Chromium based superalloys.....	9
2.3 Additive manufacturing processes.....	17
2.4 Oxidation of superalloys.....	24
Chapter 3: Materials and Experimental Procedure.....	33
3.1 Inconel 718 specimens.....	33

3.2 Inconel 718 micro-plasma additive manufacturing	34
3.3 Inconel 718 specimen preparation	36
3.4 Inconel 718 specimen oxidation	39
3.5 SEM and EDS specimen preparation.....	40
3.6 SEM and EDS analysis	41
Chapter 4: Experimental Results and Discussion	44
4.1 As-received and as-printed microstructures.....	44
4.2 Weight change after oxidation	47
4.3 Surface oxide formation and oxidation behavior at 800°C.....	51
4.4 Surface oxide formation and oxidation behavior at 900°C.....	65
Chapter 5: Concluding Remarks	81
5.1 Effect of oxidation temperature	81
5.2 Effect of exposure time.....	82
5.3 Future Work	83
References.....	85

List of Tables

Table 1. Nominal chemical composition of Ni, Ni-Fe, and Co-based superalloys [7] [20]	13
Table 2. Role of alloying elements in nickel-base superalloys [4].....	14
Table 3. Tensile test results for Inconel 718 [62]	32
Table 4. Specification of Inconel 718 wire and baseline wrought material.....	34
Table 5. Additive Manufacturing Process Parameters.....	36
Table 6. Oxidation Experiments with AM and baseline wrought Inconel 718	39
Table 7. As-printed AM Inconel 718 composition	45
Table 8. As-received baseline wrought Inconel 718 composition	47
Table 9. Weight change of AM Inconel 718 specimens	47
Table 10. Weight change of baseline wrought Inconel 718 specimens	48
Table 11. EDS composition of surface oxide at 800°C	53
Table 12. Composition analysis for AM Inconel 718 specimens held at 800°C	55
Table 13. Composition analysis for baseline wrought Inconel 718 specimens held at 800°C	56
Table 14. Composition of AM Inconel 718 after 100h at 800°C	58
Table 15. Composition of baseline wrought Inconel 718 after 100h at 800°C	59
Table 16. Composition of AM Inconel 718 after 200h at 800°C	60
Table 17. Composition of baseline wrought Inconel 718 after 200h at 800°C	61
Table 18. Composition of AM Inconel 718 after 400h at 800°C	62
Table 19. Composition of baseline wrought Inconel 718 after 400h at 800°C	63

Table 20. EDS composition of surface oxide at 900°C	67
Table 21. Composition analysis for AM Inconel 718 specimens held at 900°C	71
Table 22. Composition analysis for baseline wrought Inconel 718 specimens held at 900°C	71
Table 23. Composition of AM Inconel 718 after 50h at 900°C	72
Table 24. Composition of baseline wrought Inconel 718 after 50h at 900°C.....	73
Table 25. Composition of AM Inconel 718 after 100h at 900°C	75
Table 26. Composition of baseline wrought Inconel 718 after 100h at 900°C	76
Table 27. Composition of AM Inconel 718 after 200h at 900°C	77
Table 28. Composition of baseline wrought Inconel 718 after 200h at 900°C	78

List of Figures

Figure 1. Gas turbine engine CFM56 used in Boeing 737 aircraft [6]	2
Figure 2. Sections of a CF6 high bypass turbofan engine used in the Boeing 787 and its material distribution [10]	6
Figure 3. Alloy composition within an advanced 3-shaft turbine engine [10]	8
Figure 4. Applications of superalloys	10
Figure 5. TEM bright field image of gamma double prime in superalloy Inconel 718 [19]	11
Figure 6. Typical microstructures of a Ni-based superalloy. (a) Spheroidal and cuboidal γ' and grain boundary carbides. (b) Spheroidal γ' and grain boundary carbides [7]	11
Figure 7. Four subgroups in which Ni-Fe-Cr based superalloys can be classified.....	15
Figure 8. Precipitations found in the microstructure of Inconel 718 [25]	16
Figure 9. Overview of AM processing principles for metallic materials	19
Figure 10. Generic illustration of AM processes: (a) powder bed system, (b) wire feed system, and (c) powder feed system [37].....	21
Figure 11. Microstructure of SLM IN 718 showing Laves phase and MC carbides [42]	23
Figure 12. Illustration of Schematic Micro-Plasma Process [48].....	24
Figure 13. Oxidation film growth curves for linear, parabolic and logarithmic.....	27
Figure 14. Schematic of the transport in the scale and the course of oxidation for diffusion-controlled (parabolic) scale growth [54].....	27
Figure 15. Schematic plot of weight change vs. time comparing isothermal and cyclic oxidation behavior of the same alloy	28

Figure 16. Surface oxides formation on AM Inconel 718 after	30
Figure 17. SLM-processed Inconel 718 SEM images showing (a) surface.....	32
Figure 18. Experimental procedure.....	33
Figure 19. Additive manufacturing process setup	35
Figure 20. Milling of AM Inconel 718 using a Sajo vertical milling attachment.....	37
Figure 21. Milling of baseline wrought Inconel 718 using CNC milling.....	37
Figure 22. Measurements of AM (a) and baseline wrought (b) Inconel 718.....	38
Figure 23. Baseline wrought (a) and AM (b) Inconel 718 specimens after removal of excess moisture.....	38
Figure 24. Baseline wrought specimens after heat treatment at 800°C for 100, 200 and 400h, respectively	40
Figure 25. Puck specimen preparation: (a) hydraulic press of Inconel 718 specimen with epoxy resin, (b) non-conditioned puck specimen, (c) auto polish of a puck and (d) conditioned puck specimen with mirror finish	41
Figure 26. Image of SEM and EDS	42
Figure 27. SEM image of as-printed AM Inconel 718 microstructure using a BSE detector with (a) 1000x and (b) 5000x magnification	45
Figure 28. SEM image of as-received baseline wrought Inconel 718 obtained using a BSE detector at (a) 1000x and (b) 5000x magnification.....	46
Figure 29. Weight change of Inconel 718 specimens at 800°C.....	48
Figure 30. Weight change of Inconel 718 specimens at 900°C.....	49
Figure 31. Square of the mass gain per unit area versus time for AM Inconel 718 oxidized in air at temperatures at 800°C and 900°C for up to 400hr	50

Figure 32. Square of the mass gain per unit area versus time for baseline wrought Inconel 718 oxidized in air at temperatures at 800°C and 900°C for up to 400hr.....	51
Figure 33. Surface oxide topography of AM and baseline wrought Inconel 718 specimens oxidized at 800°C for different times ranges.	52
Figure 34. Microstructure of AM and baseline wrought Inconel 718 specimens oxidized at 800°C for different times.	54
Figure 35. Oxide layers on AM Inconel 718 after 100h at 800°C	57
Figure 36. Oxide layers on the baseline wrought Inconel 718 after 100h at 800°C	59
Figure 37. Oxide layers on AM Inconel 718 after a 200h at 800°C	60
Figure 38. Oxide layers on the baseline wrought Inconel 718 oxide layers after 200h at 800°C	61
Figure 39. Oxide layers on AM Inconel 718 after 400h at 800°C	62
Figure 40. Oxide layers on the baseline wrought Inconel 718 after	62
Figure 41. X-ray mapping of (a) AM and (b)	64
Figure 42. Surface oxide topography of AM and baseline wrought specimens Inconel 718 oxidized at 900°C for different times ranges.	66
Figure 43. Microstructure of AM and baseline wrought Inconel 718 specimens oxidized at 900°C for different times ranges.	69
Figure 44. Oxide layers on AM Inconel 718 after 50h at 900°C	72
Figure 45. Oxide layers on the baseline wrought Inconel 718 after 50h at 900°C	73
Figure 46. Oxide layers on AM Inconel 718 after 100h at 900°C	74
Figure 47. Oxide layers on the baseline wrought Inconel 718 after 100h at 900°C	75
Figure 48. Oxide layers on AM Inconel 718 after 200h at 900°C	77

Figure 49. Oxide layers on the baseline wrought Inconel 718 after 200h at 900°C 78

Figure 50. X-ray mapping of (a) AM and (b) Baseline wrought Inconel 718 after 200h at 900°C 79

Nomenclature

2D – Two-Dimensional

3D – Three-Dimensional

AM – Additive Manufacturing

ASTM – American Society for Testing and Materials

BSE – Backscattered Secondary Electron

CAD – Computer Assistive Design

CNC – Computer Numerical Control

DED– Direct Energy Deposition

DMD – Direct Metal Deposition

DMLS – Direct Metal Laser Sintering

EB – Electron Beam

EBF – Electron Beam Free-Form Fabrication

EBM – Electron Beam Melting

EOS – External Oxidation Scale

GE – General Electric

HIP – Hot Isostatic Pressing

HT – Heat Treatment

IN – Inconel

IOZ – Internal Oxidation Zone

LAW – Laser Arc Welding

LBM – Laser Beam Melting

LENS – Laser Engineered Net Shaping

LF3 – Laser Freeform Fabrication

LMD – Laser Metal Deposition

LOM – Laminated Object Manufacturing

MC – Molecular Carbides

PBF – Powder Bed Fusion

PWHT – Post-Weld Heat Treatment
PWR – Pressurized Water Reactor
SAC – Strain Age Cracking
SE – Secondary Electron
SEM – Scanning Electron Microscopy
SiO₂ – Silicon Carbide
SL – Sheet Lamination
SLM – Selective Laser Melting
SLS – Selective Laser Sintering
SMD – Shaped Metal Deposition
STL – Stereolithography
TCP – Topologically Closed Packed
UAM – Ultrasonic Additive Manufacturing
UC – Ultrasonic Consolidation

Greek symbols

γ – Gamma phase (FCC structure)
 γ' – Gamma prime precipitation hardening phase in Ni-based superalloys (Ni₃Al)
 γ'' – Gamma double prime precipitation hardening phase (Ni₃Nb)
 δ – Delta phase (Ni₃Nb)

Chapter 1: Introduction

In this chapter the motivation, the objectives and the general structure of the thesis is provided.

1.1 Preamble

Additive manufacturing (AM), previously known as rapid prototyping, utilises computer-aided-design (CAD) software to create precise geometries by fusing metals or plastics to form near-net designed shapes. Thousands of bonded superfine layers give rise to three-dimensional (3D) products where designs that could not be manufactured in one single piece by traditional processes can now be developed. AM has the advantage of producing complex shapes without the need to weld, machine or assemble individual components together. With AM technology, replacement parts can be manufactured in real-time with little to no wait-time and repair can be accomplished without disassembly or special tooling [1]. This revolutionary technology reduces turnaround time and is more environmentally friendly than traditional manufacturing methods as it prints only where material is needed with no waste generation. However, improvements are still needed to increase strength, fatigue life, stiffness and corrosion resistance of AM materials [2] and to improve the energy efficiency of AM systems.

The adaptation of AM materials to aerospace manufacturing processes initiates with a design phase, followed by prototyping and testing and securing the appropriate certification; these are in addition to any operations and maintenance requirements. In terms of materials, an aerospace engineer can choose to work with a variety of metals (>65,000), plastics (>15,000), ceramics (>10,000), and composites [3]. However, only

about 0.05% of available materials in the market are suitable for airframe and engine components [3] due to the high operating temperatures of 1300 to 1600°C [8].

Gas turbine engines have precise and complex geometries (Figure 1) that require many components [4] of different materials; e.g. lower-temperature sections are typically constructed from ferritic steels and titanium alloys, while nickel-base alloys dominate the combustor and turbine sections. Gas turbines have been used for multiple applications, such as aircrafts, electric power generation, mechanical drive systems, pump drives for gas or liquid pipelines, chemical industry, and land and sea transportation [5]. In general, aircraft and gas turbine engines require materials that are lightweight, high strength, damage tolerant, are high temperature capable, are oxidation resistant and corrosion resistant; superalloys are suitable materials to meet these needs.

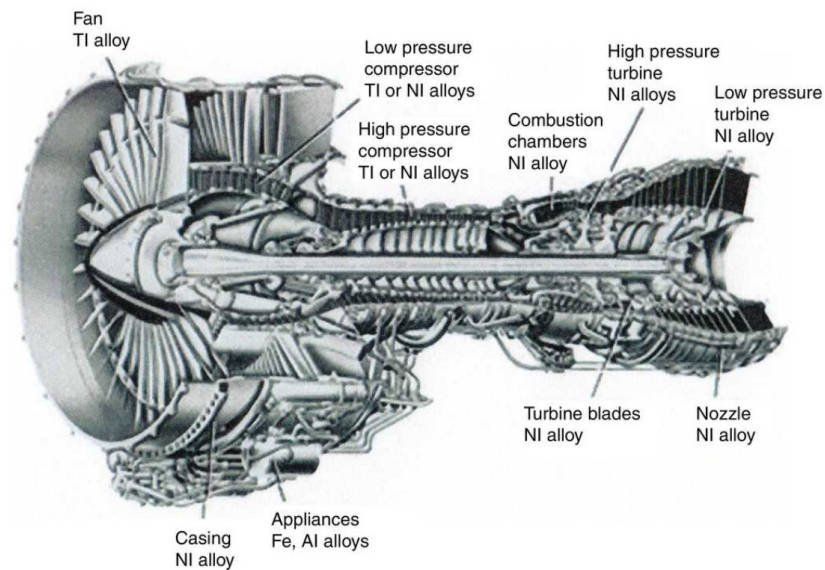


Figure 1. Gas turbine engine CFM56 used in Boeing 737 aircraft [6]

Superalloys are Ni, Ni-Fe or Co-based alloys that date back to the nineteenth century and have become increasingly popular, as they represent a wide market when it comes to the

energy and aviation sector. Superalloys can be forged, rolled to sheet, or otherwise produced in a variety of shapes [7]. Cutting edge technology and ongoing research are pushing for efficient superalloys that can decrease fuel consumption and toxic emissions in aircrafts. Robust, repeatable processes and consequently the mechanical properties of the end product are critical for the success of AM manufacturing; suitable inspection methods to ensure that the required levels of quality and performance are met are also required for this revolutionary technology.

1.2 Objective

The main purpose of this thesis is to demonstrate that additively manufactured Inconel 718 metallic components present the same oxidation behaviour as wrought Inconel 718 components at high temperatures.

1.3 Thesis structure overview

This thesis is organized into five chapters; a description of each chapter is provided below.

Chapter 1: Introduction – The advantage of AM technology and its potential applications for lightweight and durable aerospace components is discussed along with some challenges for AM technologies.

Chapter 2: Literature Review – The intent of this chapter is to provide a general introduction to gas turbines and the operating environment for different components, superalloys, the use of AM technologies for the manufacturing of superalloy components and the oxidation behaviour of these materials. It includes an introduction to Inconel 718, its microstructural characteristics and high temperature oxidation behaviour.

Chapter 3: Materials and Experimental Procedure - This chapter details the material specifications and process parameters for AM and wrought Inconel 718 material used, as well as the methods for the preparation of specimens and the procedures used to evaluate the microstructure of the material (scanning electron microscopy (SEM) and electron dispersive spectroscopy (EDS)).

Chapter 4: Experimental Results and Discussion –The surface oxide formation and microstructure changes within the interior of the AM Inconel 718 and baseline wrought Inconel 718 are presented in this chapter in a sequence of as-received material and materials oxidized at different temperatures. Also provided in this chapter is the weight changes of both alloys as a function of temperatures and duration. Comparison of the oxidation behaviour of materials examined in this study with that published in the literature is also presented.

Chapter 5: Concluding Remarks – This chapter summarizes key findings and proposed future work.

Chapter 2: Literature Review

2.1 Gas turbines and operating environments

There are two basic types of gas turbines - aeroengines and industrial power turbines. The main difference between the two types of gas turbines is their start up time and also the operating cycles [8]. In general, turbine engines operate by drawing air (-50 to 40°C) from the inlet side where it is compressed (reaching temperatures of 300–650 °C), and then mixed with fuel and burned in the combustion section, as can be seen in Figure 2. The combustion products, with gas temperatures often in the range of 1400–1500 °C, are expanded in a turbine section and the power generated is used to run the compressor and fan, in addition to providing thrust (e.g. an aircraft engine) or driving a generator (e.g. power generation). Efficiency in gas turbine engines depend on the turbine inlet temperature (TIT). Today's gas turbine engines can experience turbine inlet temperatures in excess of 1500°C. A higher TIT enables the advantageous progression of critical design parameters such as reduced fuel consumption, increased range, reduced exhaust emission and increased load-carrying capacity [9].

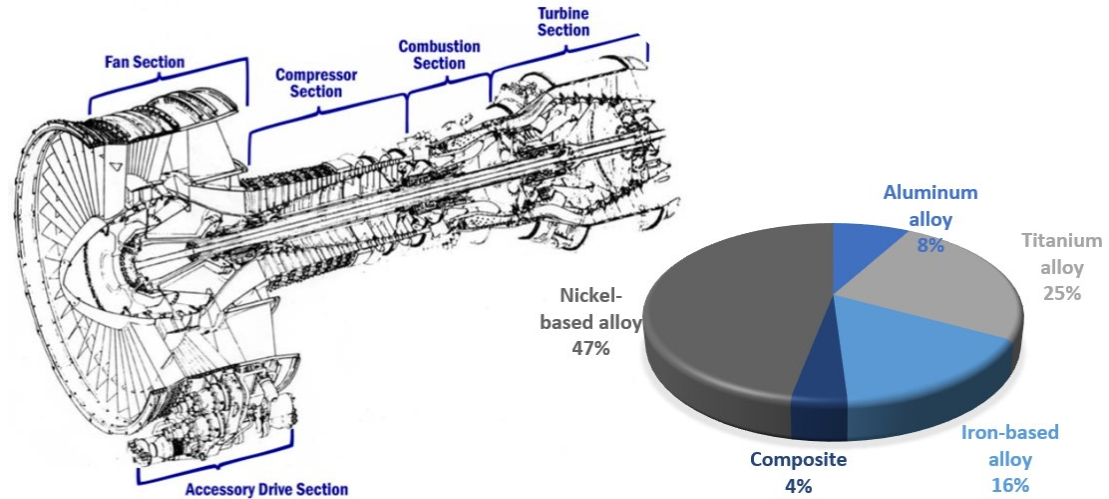


Figure 2. Sections of a CF6 high bypass turbofan engine used in the Boeing 787 and its material distribution [10]

After World War II, the future of jet engines became very promising due to their great thrust, compact size and the simplicity in their overall layout. Dr. Hans von Ohain, a German physicist, and Sir Frank Whittle are recognized as the co-inventors of the jet engine. Frank Whittle was in fact the first to patent the W.1 turbojet engine in 1930 and his turbojet engine powered the Gloster E28/29 aircraft [5]. Hans von Ohain, considered the designer of the first operational jet engine, was the second to register a patent for the turbojet engine in 1936; his He S-3 engine was the first to fly on the He178 German aircraft on August 27, 1939. Supersonic aircrafts were used later on for the Cold War in the 1960s. These aircrafts were made with special titanium and aluminum superalloys that were capable of withstanding high temperatures ($< 500^{\circ}\text{C}$) during flight without the materials softening (property degradation).

The mechanical properties of materials used in aero engines need be such that they withstand very demanding environments while under stress [10]. These materials need to

be lightweight, of high strength, damage and high temperature tolerant, and also oxidation and corrosion resistant. The mechanical properties in any given material used are determined by its chemistry, microstructure and the manufacturing process. Very often the manufacturing processes of specific materials (including superalloys) used in various parts of gas turbine engines became proprietary information.

Materials used in gas-turbine engines vary depending on the application. Modern gas turbine engines are complex machines built with alloys capable of withstanding severe service conditions which induces different failure modes such as creep, thermal mechanical fatigue, oxidation and hot corrosion [11]. Due to their excellent resistance to high temperature and their ability to maintain the strength after extended high temperature exposure [12], superalloys, Ni, Fe-Ni or Co-based, are commonly used in aeronautical and aerospace applications, particularly for turbines and compressors. Ni-based superalloys typically constitute 40–50% of the total weight of an aircraft engine and are used most extensively in the combustor and turbine sections of the engine as shown in Figure 2 [13]. Titanium superalloys are the second major constituent, representing a quarter of the total weight in aircraft engines, followed by iron-based superalloys which represent 16% weight.

Figure 3 shows the materials utilized in an advanced 3-shaft high bypass ratio commercial engine. Nickel-based superalloys represent the highest-temperature components of the engine operating at temperatures of up to 1100 °C (approaching ~90% of the temperature where the onset of melting occurs) [14]. Wrought and cast nickel-base superalloys, such as Inconel 718 and Waspaloy (Ni-based age hardenable alloy) are being used along with many other alloys. Aluminum alloys are of low density, but they are constrained in strength and temperature making them only suitable for the fan section. The later stages of the

compressors have a temperature range that only allows titanium alloys, with low-density and acceptable strength and other temperature properties. Similar demands in alloys are required for compressor blades and vanes, where traditionally no cooling schemes are used to mitigate the increasing temperatures on the later stages of the compressor [10].

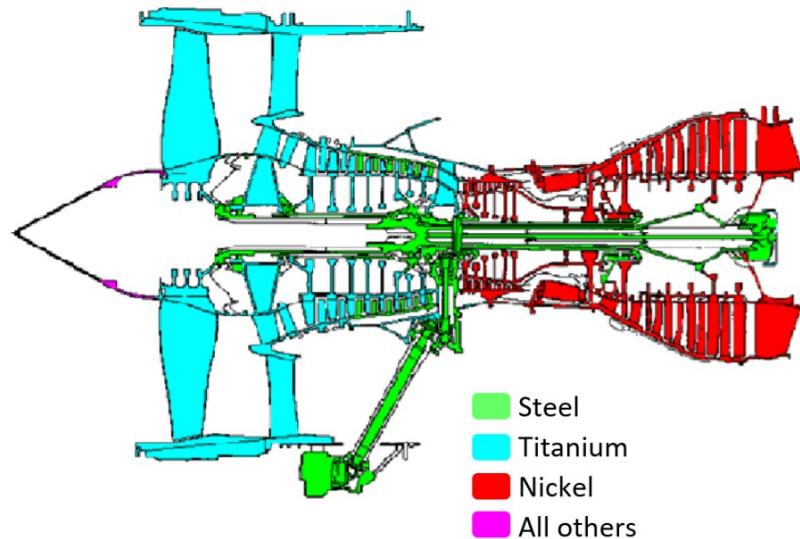


Figure 3. Alloy composition within an advanced 3-shaft turbine engine [10]

In the gas turbine, the combustion and turbine parts are continuously in contact with hot fluid. The higher the firing temperature in the combustion process, the higher the turbine efficiency and the energy output. The first generation of gas turbine engines needed to withstand operating temperatures of 800°C; nowadays, they must withstand operating temperatures of up to 1600°C (in combination with internal cooling and thermal barrier coatings). Such high firing temperatures can only be achieved by employing improved superalloys including Inconel 718 for components such as combustor, nozzles, rotating blades, turbine wheels and spacers [8].

2.2 Nickel and Nickel-Chromium based superalloys

The term "superalloy" was first coined after World War II. Nickel (Ni), cobalt (Co) or nickel-iron (Ni-Fe) based precipitation-strengthened alloys were often referred to as "superalloys" due to their high strength and corrosion resistance at high temperatures (over 540°C). Superalloys are made of relatively heavy materials, with densities in the range of 7.8 to 9.4 g/cm³ depending on the alloying elements used; with elements such as Al, Ti, and Cr reducing the density while other elements such as W, Rh, and Ta increasing density [15].

These alloys are typically manufactured in cast form due to the ease of production. Production and processing of superalloys start by melting metallic materials at very high temperatures; nickel at 1453°C, cobalt at 1495°C, and iron at 1537°C. In the early days, the lack of knowledge in heat treatment and impurities caused large differences in properties among production lots [9]. Unwanted elements, such as Bi, Pb and S, usually led to the formation of oxides, nitrides, and sulfides which weakened the alloys. Today, in order to obtain superalloys with exceptional properties, crystal orientation, grain size and shape, porosity and process parameters are strictly controlled.

Aviation gas turbines make up to 75% of all applications of superalloys, the other 25% goes to power-generation gas turbines, chemical industry, medical industry, and various other applications as seen on Figure 4, that require high temperature and/or chemical resistance [16]. Superalloys facilitate improved operating efficiency and reduce environmental emissions [17].

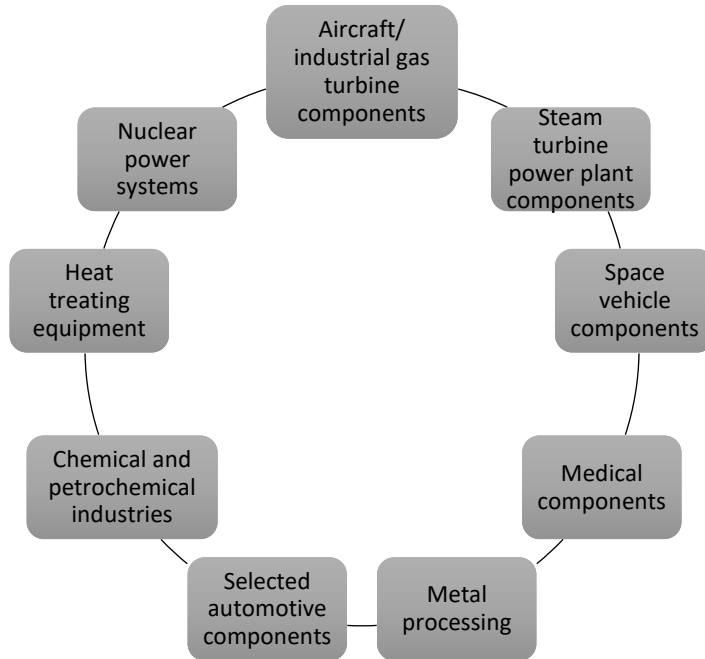


Figure 4. Applications of superalloys

The essential elements in precipitation hardenable Ni-based superalloys are Al, Ti and Nb, with a total concentration of less than 10 at.%. This generates a two-phase equilibrium microstructure, consisting of gamma (γ) and gamma-prime (γ') or gamma double prime (γ'') phases. Gamma prime (γ' - Ni₃Al or Ni₃Ti) and gamma double prime (γ'' -Ni₃Nb) are the primary precipitation-strengthened precipitates, achieving an ultimate tensile strength in excess of 1380 MPa and 0.2% offset yield strengths over 1035 MPa [18]. It is the γ' and γ'' precipitates which are largely responsible for the elevated-temperature strength of the materials.

Experimental results have shown that the morphology of gamma prime depends on the Mo content and Al/Ti ratio in iron-nickel-based alloys as shown in Figure 5. With increasing γ/γ' mismatch due to alloying, the shape changes according to the following order:

spherical, globular, blocky, cuboidal (Figure 6). When the γ/γ' lattice mismatch is high, extended exposure above 700°C (1290° F) causes undesirable phases to form [7].

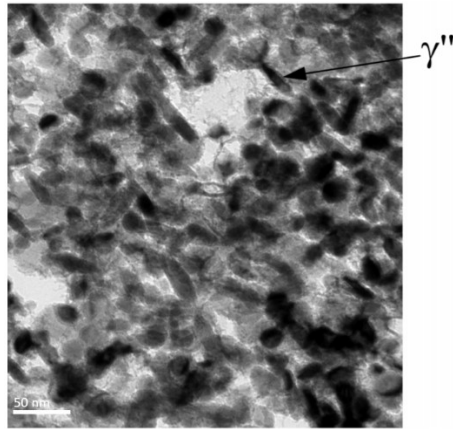


Figure 5. TEM bright field image of gamma double prime in superalloy Inconel 718 [19]

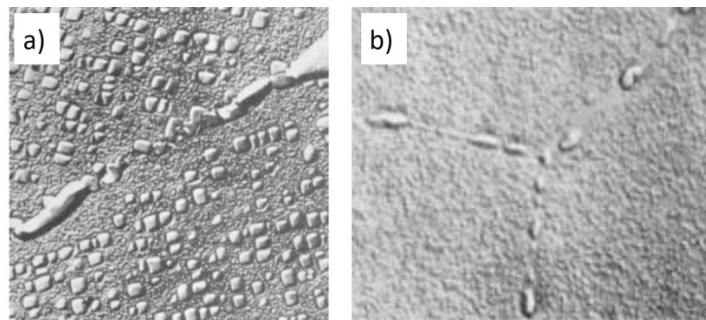


Figure 6. Typical microstructures of a Ni-based superalloy. (a) Spheroidal and cuboidal γ' and grain boundary carbides. (b) Spheroidal γ' and grain boundary carbides [7]

2.2.1 Nickel-based superalloys

Ni-based alloys play an important role in the engineering field, due to their applicability in a wide range of environments such as aqueous and atmospheric; they are often named by their trade names or by their alloy number. For instance, HASTELLOY® C-22 and INCONEL® 718 are also known as Alloy C-22 and Alloy 718 respectively. The Ni-Fe-

based superalloys, such as Inconel 718, are an extension of stainless-steel technology. Alloy 718 was patented on July 24, 1962 by Herb Eiselstein to meet the demands of emerging jet engine technology. The original Inconel alloy was a trademarked alloy family developed and marketed by Huntington Alloys in the former years of the superalloy industry, its chemistry was Ni 78%, Cr 14.5%, Fe 7%, C 0.05%, and closely resembling today's Alloy 600 [17].

Nickel is the major constituent in Ni-based superalloys, possessing a face-centered cubic (FCC) structure. Commercially pure nickel alloys containing primarily nickel (> 99 wt%), such as Alloy 200 or 201 have low strength and hardness values. In commercial superalloys, there are usually five to ten other elements, as summarized in Table 1.

These alloys are generally complex in composition, typically having at least 5 major and some minor alloying elements for the control of grain structure and mechanical properties. For example, additions of Al, Cr and Y typically improve oxidation and corrosion behavior by forming an adherent alumina/chromia scale [13].

Table 1. Nominal chemical composition of Ni, Ni-Fe, and Co-based superalloys [7] [20]

Chemical compositions (% by weight)						
Designation	Ni	Cr	Mo	Fe	Cu	Other
Nickel 200	99.6					C 0.04
Nickel 201	99.6					C 0.02 max.
Monel alloy 400	65.1			1.6	32.0	Mn 1.1
Monel alloy K-500	64.7			1.0	30.2	Al 2.7, Ti 0.6
Inconel alloy 600	76.0	15.0		8.0		
Inconel alloy 617	56.0	24.0	10.0	3.0	0.5	Co 15.0, Al 1.5, Ti 0.6, Si 0.5, C 0.15, S 0.015, P 0.015
Inconel 622	59.0	20.5	14.2	2.3		W 3.2
Inconel alloys 625 and 625LCF	61.0	21.5	9.0	2.5		Nb 3.6
Inconel 686	58.0	20.5	16.3	<1.0		W 3.8
Inconel 690	61.5	29.0		9.0		
Inconel 713	Rest.	14.0	5.2	2.50 max.	0.50 max.	Al 6.5, Ti 1.0, C 0.2, Si 0.5 max; Mn 0.25 max.
Inconel 718	54.0	18.0	3.0	18.5		Nb 0.5, Ti 1.0
Inconel 725	57.0	21.0	8.0	7.5		Nb 3.5, Ti 1.5, Al 0.3
Inconel 738C	Rest.	16.3	2.0	0.50 max.		Nb 1.1, Co 9.0, Al 3.7, Ti 3.7, C 0.13, W 2.8, Ta 2.0, B 0.012, Zr 0.08, Al+Ti 7.2; Si 0.3 max; S 0.015 max; Mn 0.2 max.
Inconel X-750	70.0	17.0		9.0	0.5	Nb 1.2, Co 1.0, Mn 1.0, Al 1.0, Ti 2.75, Si 0.5, C 0.8, S 0.01
Inconel C-276	57.0	16.0	16.0	5.5		W 4.0
Inconel G-3	44.0	22.0	7.0	19.5	2.0	
Inconel 050	50.0	20.0	9.0	17.0		
Inconel 800	32.5	21.0		46.0		C 0.05
Inconel 825	42.0	21.5	3.0	28.0	2.0	
Inconel 864	34.0	21.0	4.2	39.0		Si 0.8, Ti 0.6
Inconel 925	44.0	21.0	3.0	28.0	1.8	Ti 2.1, Al 0.3
Inconel 020	35.0	20.0	2.5	37.0	3.5	Nb 0.6
Inconel 028	32.0	27.0	3.5		1.0	Mn 2.0
Inconel 25-6MO	25.0	20.0	6.5	47.0	0.9	N 0.20
M951	Rest.	9.0	3.0			Nb 2.2, Co 5.0, Al 6.0, C 0.05, W 3.5, B 0.024, Y 0.017
GH202	Rest.	20.4	4.1			Al 1.38, Ti 2.02, C 0.06, P 5.62
Udiment 500	Rest.	20.5	3.0			Co 19.0, Al 1.9, Ti 2.7, C 0.01
Haynes 282	Rest.	19.5	8.6	0.7		Co 10.33, Al 1.52, Ti 2.13, Si 0.06, C 0.06, S <0.002, P 0.002, B 0.005
Hastelloy X	47.0	22.0	9.0	18.0		Co 1.5, W 0.6, C 0.1, Mn 1.0 max; Si 1.0 max; B 0.008 max; Nb 0.5 max; Al 0.5 max; Ti 0.15 max
Stellite 6	2.3	28.5		2.3		Co Rest; W 4.7, C 1.1, Si 1.2
X-40	10.0	25.0				Co 54.0, W 8.0, C 0.5

The addition of alloying elements can have a significant impact on the superalloy properties. Table 2 presents a summary of the effects of different elements on the properties of nickel-based superalloys [4]. The presence of γ and γ' phases remain the major constituents in nickel-based superalloy microstructures, even with the addition of many other elements [13]. One of the disadvantages associated with γ' precipitation hardened superalloys is its poor weldability due to strain age cracking (making it difficult for 3D printing). As such new weldable materials have been researched extensively by diluting a number of alloying elements while maintaining the material's core strength and ductility. For instance, adding Co widens the alloy's solidification range [21].

Table 2. Role of alloying elements in nickel-base superalloys [4]

Effect	Alloying Elements
Solid-solution strengtheners	Co, Cr, Fe, Mo, W, Ta, Re
Carbide formers:	
MC	W, Ta, Ti, Mo, Nb, Hf
M ₇ C ₃	Cr
M ₂₃ C ₆	Cr, Mo, W
M ₆ C	Mo, W, Nb
Carbonitrides: M(CN)	C, N
Forms γ' Ni ₃ (Al, Ti)	Al, Ti
Raises solvus temperature of γ'	Co
Hardening precipitates and/or intermetallics	Al, Ti, Nb, Ta
Oxidation resistance	Al, Cr, Y, La, Ce
Improve hot corrosion resistance	La, Th
Sulfidation resistance	Cr, Co, Si
Improves creep properties	B, Ta
Increases rupture strength	B
Grain-boundary refiners	B, C, Zr, Hf
Retard γ' coarsening	Re

2.2.2 Ni-Fe-Cr-based superalloys

Ni-Fe-Cr-based superalloys can be further classified into four groups: γ' -strengthened alloys, γ'' -strengthened alloys, low-expansion alloys and solid solution alloys. A summary of each group can be found in Figure 7.

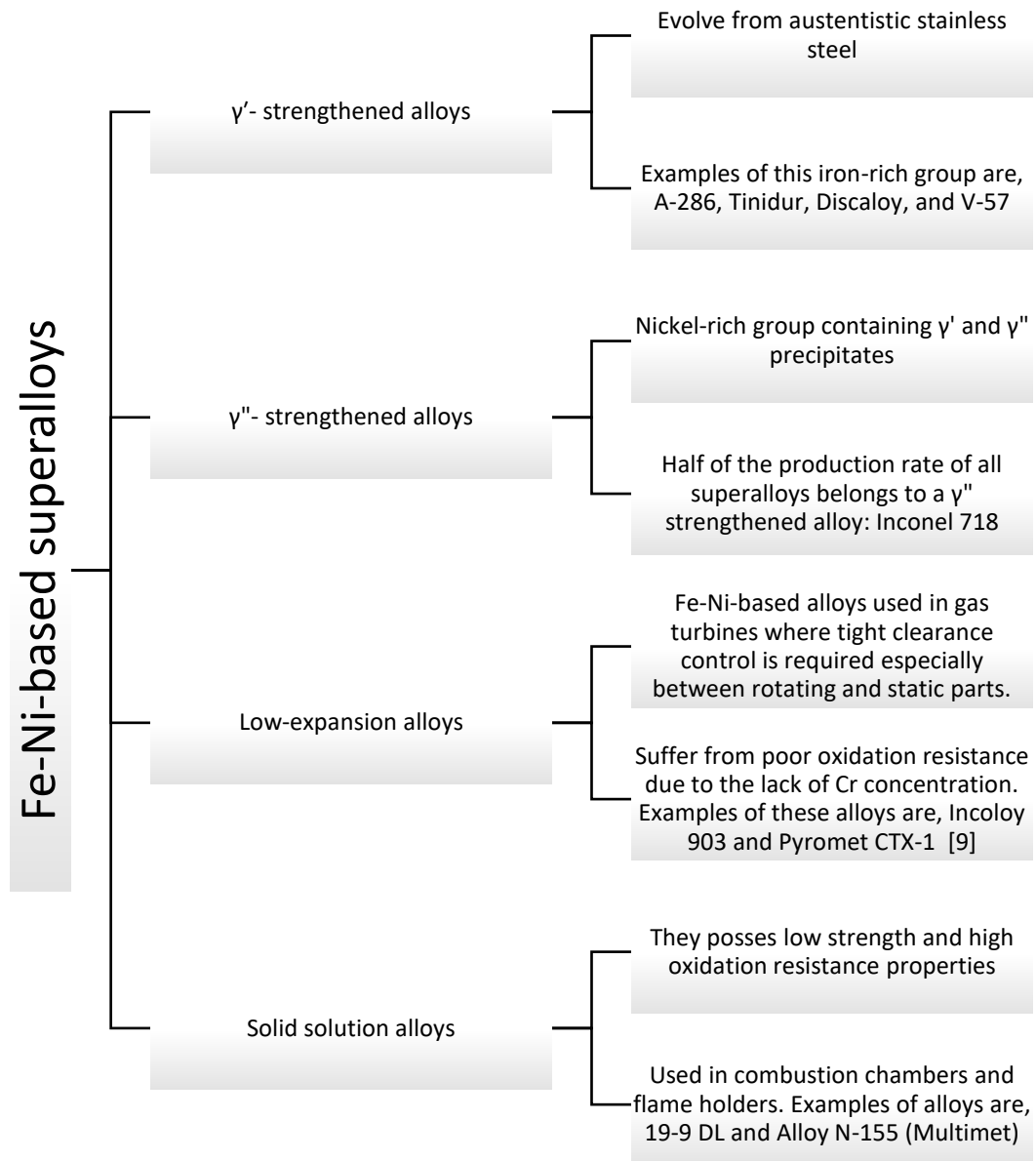


Figure 7. Four subgroups in which Ni-Fe-Cr based superalloys can be classified

Inconel 718, a nickel-iron-chromium-based superalloy, is the main focus of this research. It was first evaluated by General Electric (GE) in terms of its mechanical properties and weldability, as replacement for highly alloyed steels. In January 1965, GE and other industries made the commitment to commercialize Inconel 718. It took over a decade of effort and resources before it was debuted on the GE-1 Core Engine Program and later on became widely used in many other applications, such as TF39 Military, CF6 Commercial Aircraft (Figure 2), LM2500 and 5000 Marine and Industrial engines as compressor blades/vanes and turbine frames and casings that are still ongoing [22]. Inconel 718 is perhaps the most widely used alloy with a production rate of roughly half of all superalloys in the world. In fact, nearly one-third of the materials in a GE CF6 engine consist of Inconel 718. It has a temperature range that is limited to about 650°C [23] for very long term applications such as in a power generation turbines but superior stress carrying characteristic; some of its applications include rear stages of compressor blades and vanes, shafts, supports, casings, and so on [17]. Unavoidable impurities in trace amounts are often found in molten Inconel 718. When melted properly to produce low levels of impurities, this alloy presents tremendous design opportunities due to excellent fatigue life at service temperatures greater than 760°C [24] [12].

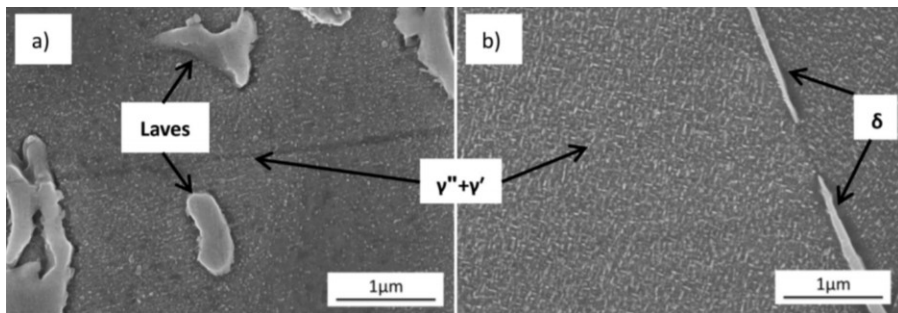


Figure 8. Precipitations found in the microstructure of Inconel 718 [25]

One major concern in the design of new superalloys is the appearance of topologically closed-packed (TCP) phases such as Laves phases are often found in iron-nickel based superalloys (Figure 8). Laves phases are detrimental to the properties of the alloys and are rich in refractory alloying elements (assume complex hexagonal crystal structures). It is detrimental to the properties of the alloys. Its chemical composition assumes a form of A_2B where A represents Ni, Cr, Fe, and B represents Nb, Mo, Si and Ti in iron-nickel alloys [26]. Laves formation is promoted by high temperatures, stress, and time.

Depending on the chemical and physical processes used in fabricating Inconel 718, it could include phases such as γ' -, γ'' - and δ -phases, and minor secondary phases such as Laves phases and carbides and/or nitrides [27]. Because the gamma double prime precipitate forms more slowly than gamma prime, Inconel 718 is generally immune to strain age cracking (SAC) during post weld heat treatment (PWHT) [18].

2.3 Additive manufacturing processes

Additive manufacturing (AM) technology, also known as three-dimensional (3D) printing, builds parts from powder, wire or sheets by progressively adding thin layers on top of each other. Additive manufacturing technologies have gained momentum in the last decade and offer a broad range of advantages compared to conventional manufacturing techniques like casting, forging, or machining [28], providing one of a kind complex parts of different materials [29]. It is suitable for applications where low volume and high value parts are required, such as the aerospace and medical industry; and it also enables on-demand manufacturing with un-surpassed responsiveness and promotes a reconfigurable, agile manufacturing supply chain [30]. For these reasons, AM has progressed rapidly in recent

years from prototyping to end-use products, reaching a projected \$21 billion market by 2020 [31].

This technology allows the production of complex or customized parts directly from the CAD design without the need for expensive tooling or forms such as punches, dies or casting molds and reduces the need for many conventional processing steps. Intricate parts true to their design can be made in one-step [32]. In summary, 3D printing provides flexibility in design, material savings, as well as customisation and individualism [33].

2.3.1 Components of AM Systems

A typical AM system consists of a heat source, a motion guidance system, a wire/powder delivery system, a carrier-gas delivery system, and sensors for feedback control. An energy source, i.e. a laser, electron or plasma arc, provides the heat to melt part of a substrate located on a build platform, creating a tiny melt pool. The substrate is either a sacrificial foundation or a pre-existing part (such as a worn forming die or a damaged part) that requires further material additions [34]. For additive manufacturing processes, the feedstock (the bulk raw metallic material that is fed into the process) can come in the form of powder (dry, paste or slurry), filament, or sheet [35]. Many factors can affect the final product's surface finish, dimensional accuracy, microstructure integrity and mechanical properties, including power, relative traverse speed and pattern of power source (head or nozzle), powder/wire feed rates, deposition orientation and so on.

2.3.2 Classifications

Additive manufactured processes can be classified into three broad categories based on the process used for the production of metallic parts: Direct Energy Deposition (DED), Power Bed Fusion (PBF), and Sheet Lamination (SL), as represented by Figure 9.

- Direct Energy Deposition (DED) processes use a laser or electron beam to melt powders or wires as their being deposited. They can be referred to as Laser Engineered Net Shaping (LENS), Direct Metal Deposition (DMD), Laser Metal Deposition (LMD), Laser Freeform Fabrication (LF3), Shaped Metal Deposition (SMD), and Electron beam free-form fabrication (EBF). Some of the disadvantages associated with DED processes are the need for a support structure (hence post AM material removal), part geometry/complexity, rougher surface finish and higher cooling rates.

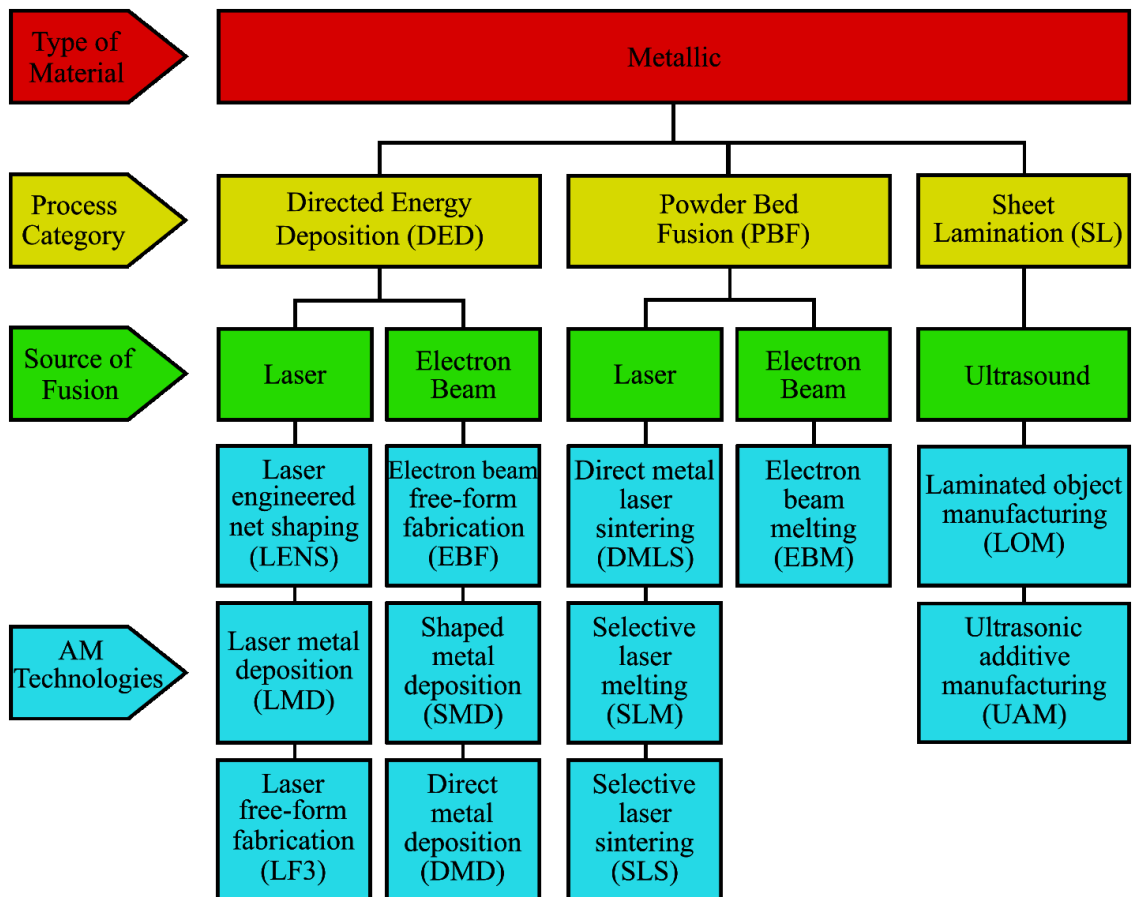


Figure 9. Overview of AM processing principles for metallic materials

- In Powder Bed Fusion (PBF) technology the energy source can be either a laser or electron beam. PBF includes the following printing techniques: Direct Metal Laser Sintering (DMLS), Electron Beam Melting (EBM), Selective Laser Melting (SLM) and Selective Laser Sintering (SLS). SLS and DMLS operate by merging the particles in the material, without achieving a full melt. SLS is used to describe the sintering process when applied to non-metal materials and DMLS is used for metal materials.
- Sheet Lamination (SL) processes can build material sheets through two processes: Laminated Object Manufacturing (LOM) and Ultrasonic Additive Manufacturing (UAM). LOM generates material sheets using a layer-by-layer lamination process. Sheets can be either cut and then bonded together or bonded and then cut. UAM or Ultrasonic Consolidation (UC), is a relatively new hybrid sheet lamination process that combines ultrasonic sheet welding with CNC milling. Multiple-layered parts are built from bottom to top on a rigid base plate and milled afterwards.

Metal Additive manufacturing processes [36] can also be categorized based on their feed mechanisms as: powder bed systems, powder feed systems and wire feed systems. These three categories are based on material feed stock, energy source, build volume, and so on (Figure 10).

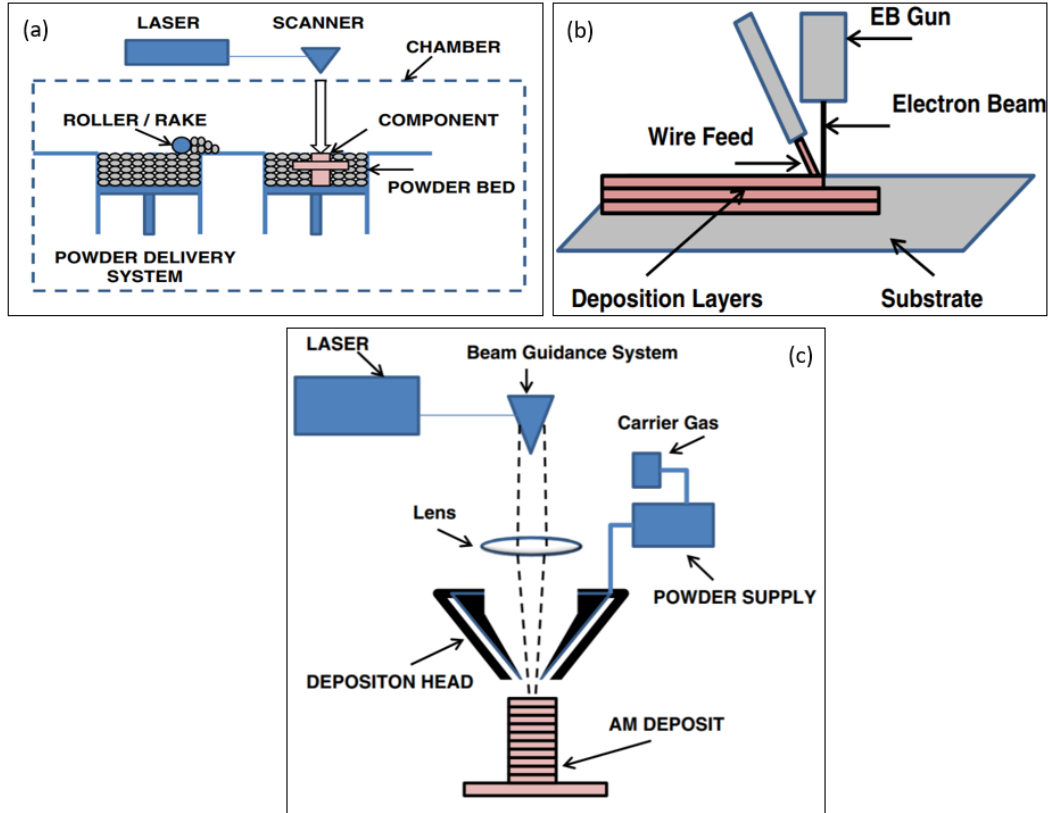


Figure 10. Generic illustration of AM processes: (a) powder bed system, (b) wire feed system, and (c) powder feed system [37]

In a powder bed system, a 3D model is created and sliced into 2D slices. The powder is melted after being injected into the melt pool on the substrate, as shown in Figure 10.a. The process repeats itself until the completion of the part. Wire feed systems start with a 3D CAD model which then is converted into CNC code. In the example shown in Figure 10.b, the electron beam gun deposits metal, via the wire feedstock, layer by layer, until the part reaches near-net shape. Once the part reaches near-net shape, it undergoes heat treatment and machining [38]. Finally, direct powder feed is similar to the wire feed system as the material is deposited where it is needed. Figure 10.c shows how the powder delivery system deposits a steady and precise stream of powder through a single nozzle into the melt

pool. Further classification of metal additive manufacturing processes can be done as a function of the heat source (electron beam, laser or arc) [39].

2.3.3 Materials and Microstructure

Despite its potential applications in different fields, only a limited number of metallic alloy systems are currently available for high quality additive manufacturing: pure titanium, Ti6Al4V, 316L stainless steel, 17-4PH stainless steel, 18Ni300 maraging steel, AlSi10Mg, CoCrMo, and Nickel-based superalloys like Inconel 625 and Inconel 718 [39] [40]. Some of the challenges with using AM technologies are the material composition in-homogeneity in the printed parts and the formation of voids, microcracks and lack of fusion in laser sintering/melting parts [41]. In particular, the resultant microstructures have shown to differ drastically from those of wrought materials. Hot isostatic pressing (HIP) is often required for post processing to improve mechanical properties by the dissolution of undesirable phases as well as pore closures [42].

Two main challenges are encountered when manufacturing Inconel 718 SLM components. First, Inconel 718 contains fine MC-type carbides and eutectic γ /Laves phase segregated in interdendritic regions as seen in Figure 11; these eutectic reaction products happen when the concentration of Nb, Mo, C in the remaining melt is sufficiently high ($\sim 850^\circ\text{C}$) [42]. The use of a high energy laser can result in irregularly shaped Laves phases rich in Nb and Mo or porosities. Second, a post-processing heat treatment is necessary to reduce the occurrence of carbide and Laves phase. The heat treatment includes: (i) solution heat treatment to dissolve hardening phases into the matrix and (ii) aging treatment to form γ'' and γ' phases [43]. HIP-treatment to SLM manufactured Inconel 718 at 1160°C for 3 hours

has been reported to achieve complete dissolution of eutectic Laves phase; however, MC-type carbides will still remain [43].

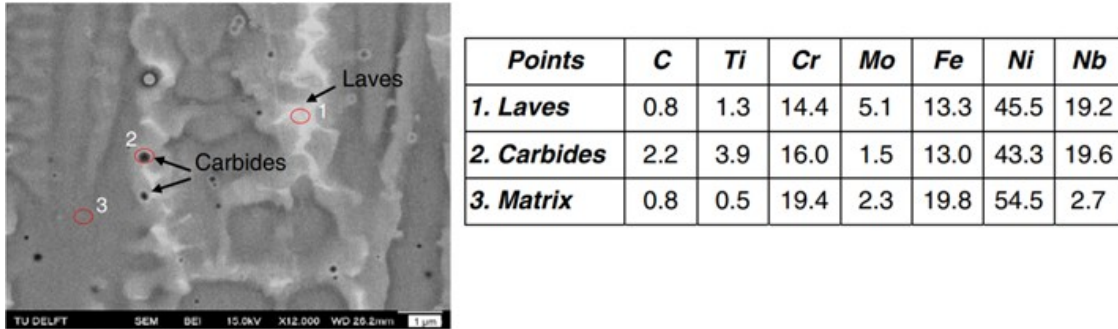


Figure 11. Microstructure of SLM IN 718 showing Laves phase and MC carbides [42]

The alternative is to use micro-plasma AM processes instead of SLM which is more cost effective and energy efficient than the laser or electron-based systems [44][45]. In addition, the deposition rate of micro-plasma process can exceed 10 times that of a laser or electron beam, in the scale of ~100 g/min. vs. 10 g/min [46][47]. Compared to other arc-based welding processes, micro-plasma transferred arc provides a cleaner weld deposit [48] due to the use of non-consumable electrodes and the presence of a secondary shielding gas system (Figure 12).

In this research, a wire material is used due to lower cost and higher material utilization rate (near 100%). Use of wire in micro-plasma additive manufacturing can also eliminate contamination from reclaimed powders and moisture entrapment.

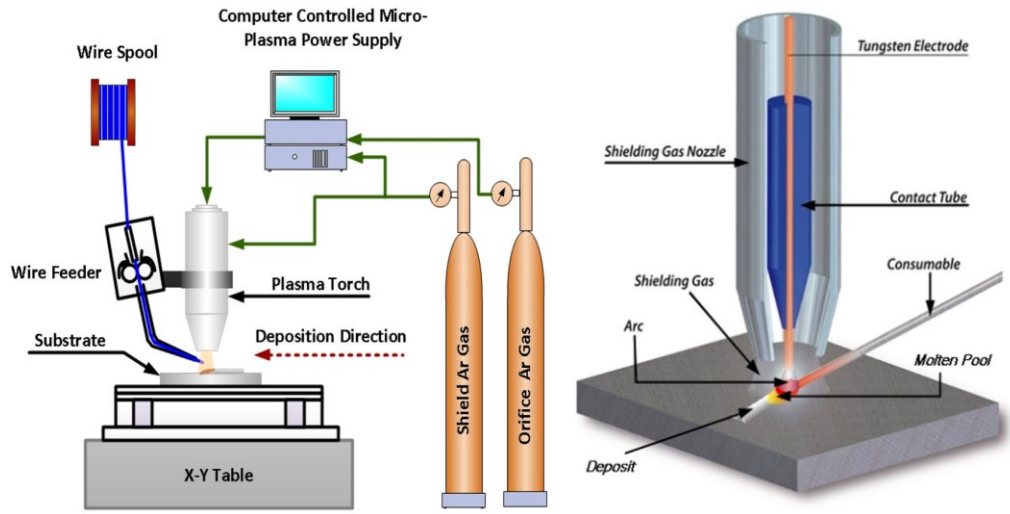


Figure 12. Illustration of Schematic Micro-Plasma Process [48]

2.4 Oxidation of superalloys

Oxidation is the chemical reaction of oxygen with a metal when it is exposed to a gas or aqueous environment. High temperature corrosion results in a considerable maintenance and replacement expenditure in various industries, including: high temperature processing, new renewable energy technologies, and other critical high temperature components (e.g. aircraft engines, turbines, and power plant boilers [49]). Its prevention is a multi-billion-dollar industry, making the oxidation resistance of superalloys a key factor when determining the suitability of alloys.

2.4.1 Rate of oxidation

During the oxidation of different metals, various empirical rate laws have been observed. The rate at which the oxidation occurs depends on the access of oxygen to the metal atoms, the temperature, and the composition, grain shape and size of the metal. The resulting oxide layer has a strong effect on the material.

Generally speaking:

1. The rate of oxidation is controlled by the rate of diffusion of oxygen or metal ions through the oxide. If oxygen diffusion is more rapid, oxidation occurs between the oxide and the metal; if the metal ion diffusion is more rapid, oxidation occurs at the oxide-atmosphere interface.
2. Oxidation rates follow an Arrhenius relationship, increasing exponentially as the temperature increases [50].
3. Pure metals at high temperature have an oxidation rate that is proportional to grain size (i.e. oxidation rate decreases with decrease in grain size, hence more grain boundary for active metal transport such as Cr, Al and Si) [51].
4. The transport mechanism of ions and electrons during the oxidation of pure metals can be explained by Wagner's theory of oxidation, i.e., the oxidation rate is controlled by both the partial ionic and electronic conductivities of oxides and the metal-oxide concentration [51].

The kinetics of oxidation of metals and alloys generally follow linear, parabolic and logarithmic reaction rates. A schematic representation can be seen in Figure 13.

(a) The linear reaction rate is based on the surface reaction step towards the reactive gases of the environment [51]. Linear oxidation occurs when the surface is porous (i.e. magnesium), in cracked oxide films or when oxygen has continued access to the metal surface. In this case, the thickness of oxide (x) formed is represented by the following equation (Equation 2.4-1), where t is time and k is a constant that depends on the type of metal and temperature.

$$x = kt \qquad \text{Equation 2.4-1}$$

The oxidation rate will remain constant through time when the oxide scale formed on the metal surface provides no protection barrier, this can occur due to oxide cracking and spalling, volatile oxides and molten oxidation products [52].

(b) In a parabolic relationship, the oxidation reaction is controlled by the diffusion of ions through the oxide scale, which is in turn controlled by the chemical potential gradient as a driving force (Equation 2.4-2). This relationship is typical for metals with thick coherent oxides, i.e. Fe, Cu and Ni.

$$x = \sqrt{k_1 t + k_2} \quad \text{or} \quad x^2 = k_1 t + k_2 \quad \text{Equation 2.4-2}$$

As the thickness of the oxide scale increases, the rate of oxidation decreases with increasing time due to the increasing diffusion distance for ions [52]. The oxidation rate is, thus, inversely proportional to the thickness of the oxide scale.

The extent of reaction may also be expressed in terms of a mass change per unit area, $\Delta m/A$, as shown in Equations 2.4-3 and 2.4-4:

$$\left(\frac{\Delta m}{A}\right)_t^2 - \left(\frac{\Delta m}{A}\right)_{t_0}^2 = 2k''(t - t_0) \quad \text{Equation 2.4-3}$$

$$k'' = \left(\frac{8}{V}\right)^2 k' \quad \text{Equation 2.4-4}$$

where V is the equivalent volume of the oxide, and the units of k'' are g^2/cm^4 .

(c) In a logarithmic relationship, the driving force for the oxidation is the electric field across the oxide film [60], as expressed by Equation 2.4-5 (where k and c are constants for a particular temperature, environment, and composition). This reaction results in the growth of thin-oxide films in the range of 2-4 nm [51] which can be protective when composed of Al and Cr.

$$x = k \ln(ct + 1) \quad \text{Equation 2.4-5}$$

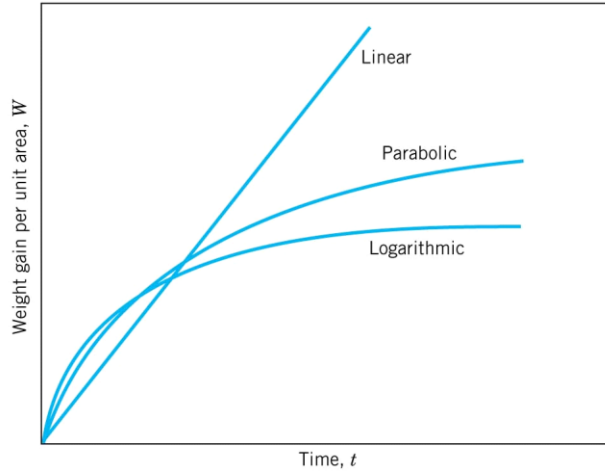


Figure 13. Oxidation film growth curves for linear, parabolic and logarithmic rate laws [50]

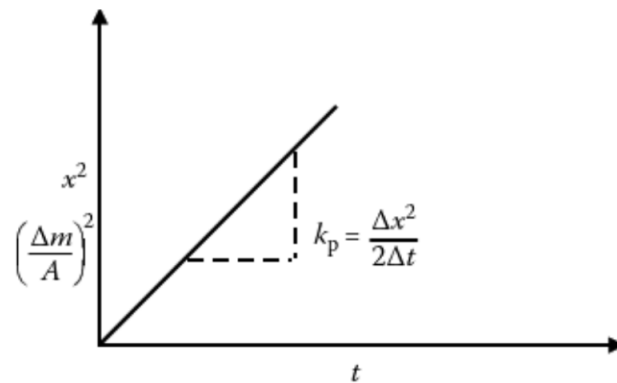


Figure 14. Schematic of the transport in the scale and the course of oxidation for diffusion-controlled (parabolic) scale growth [54]

The oxidation rate constant, k_p , is the most important parameter that describes the resistance of a material to high-temperature oxidation. The slope in Figure 14 corresponds directly to the rate constant k_p [53]; in this plot, the y-axis is the square of the measured mass change ($\Delta m/A$) or oxide thickness (x) and time (t) is plotted along the x-axis.

Oxidation, as evaluated by weight gain, behaves different in cyclic and isothermal heating environments. As shown in Figure 15, the rate of weight gain in both cyclic and isothermal oxidation is similar at the start but eventually a cyclic oxidation will reach a maximum and start to decrease. This decrease, which is due to oxide spalling, actually corresponds to a more rapid rate of consumption of the alloy [3]; Inconel 718, the focus of this research, follows an isothermal oxidation behavior.

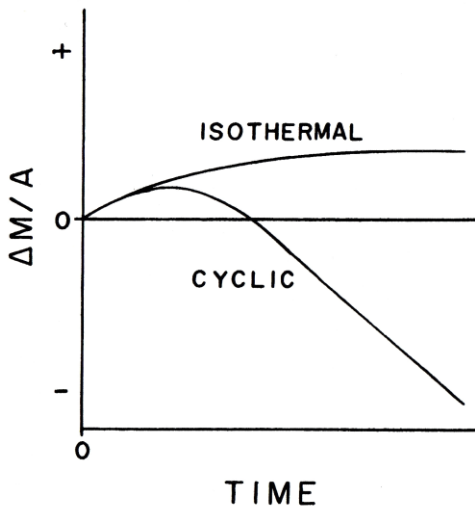


Figure 15. Schematic plot of weight change vs. time comparing isothermal and cyclic oxidation behavior of the same alloy

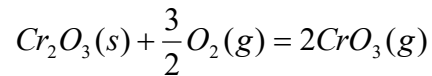
2.4.2 Types of oxidation for Ni-based alloys

A large number of Nickel-base superalloys rely on the formation of Cr_2O_3 and Al_2O_3 scales for oxidation resistance. The oxidation behavior of the Ni-Cr alloys may be separated into three types [50]:

- **Type I** – it corresponds to dilute alloys (<10%Cr). For this group the rate constant k' is somewhat larger than those for pure nickel due to the “doping” of the NiO scale with Cr, which results in an increased diffusivity of Ni ions.

- **Type II** – it corresponds to alloys with a Cr concentration ranging between 10-30%. External scales of Cr₂O₃ can be observed over alloy grain boundaries, while external NiO scales form over alloy grains with some internal Cr₂O₃ formation.
- **Type III (>30%Cr)** – For this group the rate constants are several orders of magnitude smaller than those for pure Ni.

Continuously formed protective oxide scales such as chromia (Cr₂O₃) and alumina (Al₂O₃) enable Ni-based superalloys to be exposed to air at high temperatures with minimum material loss (spallation or oxide ingression). However, alloys that form protective Cr₂O₃ scales are susceptible to accelerated degradation at very high temperatures in high p_{O2} gases due to the following reaction:



where (*s*) stands for solid and (*g*) stands for gas.

Chromia acts a protective barrier at elevated temperatures but becomes unstable above 871°C, requiring alumina to provide the protection [54]. Figure 16 is a graphical representation where one can observe different oxides on AM Inconel 718 after oxidation. Here the formation of Cr₂O₃ dominates the early stage of oxidation process.

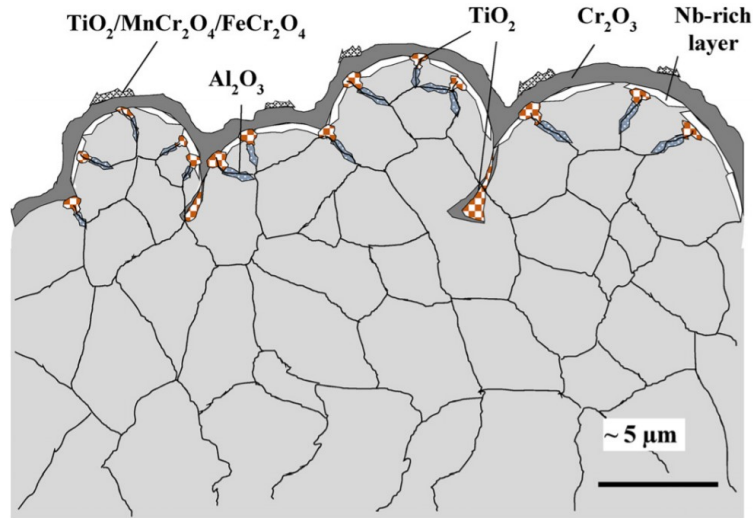


Figure 16. Surface oxides formation on AM Inconel 718 after high temperature oxidation [55]

2.4.4 Oxidation of Ni-based superalloys and Inconel 718

The growth rate and type of oxides formed in superalloys depends on multiple factors. The rate of oxide growth on a metal surface has been characterized by analyzing the effects of time and temperature on the metal structure [53]; several studies have also been conducted on Ni-based superalloys and their oxidation behaviour as a function of the manufacturing process used and service temperature; while others have attributed it to the chemical composition of the superalloy. A summary of a few is presented as follows.

Juillet et al. [56] studied AM and wrought Inconel 718 exposed to 600–800°C for a 48h period and found that a Cr_2O_3 layer developed on both materials. In wrought Inconel 718, the chromia layer appeared less compact than that on additively manufactured specimens. The oxidation behavior of a Ni-based GH202 superalloy was investigated by Cao et al. [57]. After being exposed to 800°C for 100h, oxide scales composed of Cr_2O_3 , NiCr_2O_4

and TiO_2 were observed. One of their secondary findings was that GH202 (with a composition (wt. %) of 1.38Al, 2.02Ti, 20.39Cr, 4.08Mo, 5.62W, 0.06C, and balanced Ni) has the ability to form a continuous and compact Cr_2O_3 layer at 800°C and 900°C. While at 1000°C for 150 h and 1100°C for 100h, there was spallation of the chromia layer.

Ample research has concluded that the oxidation of Inconel 718 and similar Ni-based superalloys follows a parabolic oxidation behavior that is governed by the diffusion of anions and/or cations through the external scale. Mallikarjuna et al. [58] validated this as part of the comparison of the isothermal oxidation of three Ni-based superalloys: polycrystalline cast IN738LC (low carbon alloy), single-crystal N5, and a powder metallurgy Ni-Cr-Fe alloy (with 6% Al and 0.5% Si). Sanviemvongsak et al. [55] concluded that EBM, LBM and wrought Inconel 718 followed quasi-parabolic oxidation rates. Other studies [59] [60] found that SLM Inconel 718 specimens exposed for extended time ranges at 850°C have a parabolic oxidation rate resulted from the formation of a dense, protective, and stable oxide scale on the surface of the alloy.

Jia et al. [61] investigated the oxidation behaviour of Inconel 718 as a function of SLM processing parameters and concluded that 330 J/m is the optimum laser energy density required to achieve a refined microstructure with lower mass gains (Figure 17).

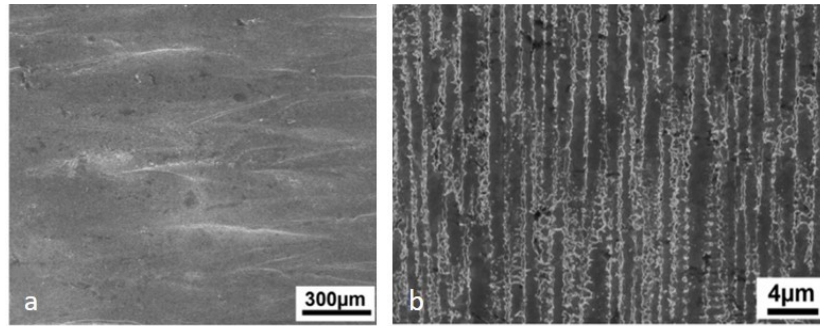


Figure 17. SLM-processed Inconel 718 SEM images showing (a) surface and (b) crystal morphology [61]

Wang et al. [62] reported that SLM printed specimens exhibited superior ductility than wrought Inconel 718 but inferior ultimate tensile strength (UTS) and yield stress (σ). However, after heat treatment, the tensile strengths and ductility of the SLM+HTed Inconel 718 at room temperature were compared with those of wrought Inconel 718; results can be found in Table 3.

Table 3. Tensile test results for Inconel 718 [62]

Sample state	$\sigma_{0.2}$ (MPa)	UTS (MPa)
SLMed	889–907	1137–1148
SLMed + HTed	1102–1161	1280–1358
Wrought IN718 (AMS) [23]	1030–1167	1275–1400

Based on the literature review, it becomes apparent that oxidation resistance plays an important part in alloy performance and selection. As such, as part of the development of new AM process to create 3D geometry, the effects of temperature and duration on the oxidation behaviour of AM Inconel 718 was evaluated and forms the main focus of this thesis. The ultimate objective is to demonstrate if a plasma arc additively manufactured specimen is equivalent to wrought Inconel 718 alloy.

Chapter 3: Materials and Experimental Procedure

This chapter details the experimental procedure that was used for this research. A general summary is presented in Figure 18.

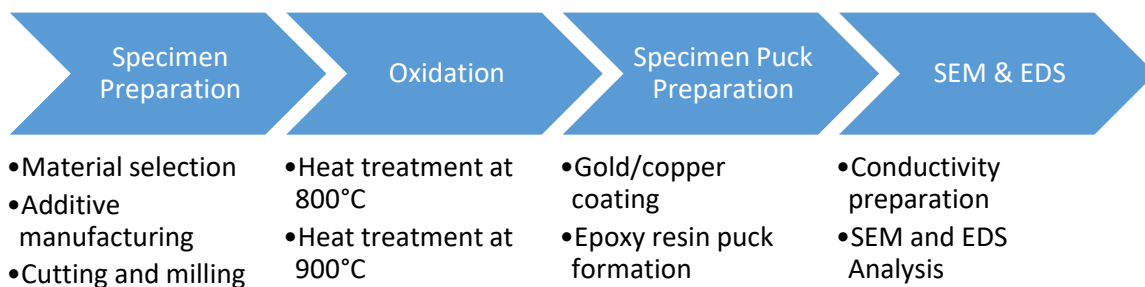


Figure 18. Experimental procedure

3.1 Inconel 718 specimens

All additively manufactured (AM) specimens studied in this research were Inconel 718 with composition summarized in Table 4. Both specimens have high concentration of Cr that promotes the formation of a protective Cr_2O_3 oxide layer and gives the alloy its oxidation and hot corrosion resistance [4]. The presence of Nb, formerly known as Columbium, in this alloy makes it free from strain-age cracking during welding.; it also presents trace amounts of aluminum and titanium which serve as a basis for possible secondary precipitation hardening.

A wrought of Inconel 718 material was used as the baseline. The baseline wrought specimen has a similar composition to the AM specimen, refer to Table 4, where the main difference in composition is trace elements which represent <3% of the final composition of the materials. High amounts of Cr (~21%) are present in the alloy, along with several other major (Ni, Fe, Nb, Mo) and minor (Ti, Si, Co) alloying elements. In addition to the

elements listed in Table 4, several trace elements are present in baseline wrought Inconel 718 such as copper, manganese, copper, sulfur, phosphorus and boron.

Table 4. Specification of Inconel 718 wire and baseline wrought material

Element	Inconel 718 wire (wt. %)	Baseline wrought Inconel 718 (wt. %)
Nickel, Ni	50 – 55	50 – 55
Chromium, Cr	17 – 21	17 – 21
Niobium, Nb	4.75 – 5.5	4.75 – 5.5
Molybdenum, Mo	2.8 – 3.3	2.8 – 3.3
Cobalt, Co		1
Titanium, Ti	0.65 – 1.15	0.65 – 1.15
Silicon, Si		0.35
Manganese, Mn		0.35
Copper, Cu		0.3
Aluminum, Al	0.2 – 0.8	0.2 – 0.8
Carbon, C		0.08
Sulfur, S		0.015
Phosphorus, P		0.015
Boron, B		0.006
Iron, Fe	Balance	Balance
Specification	ASTM B637/B670, “Turbaloy 718”	AMS 5662, ASTM B637, “Pyromet 718”
Supplier	United States Welding Corp.	Carpenter Technology Corporation

3.2 Inconel 718 micro-plasma additive manufacturing

A micro-plasma system was used to manufacture the AM specimen. In this system, an arc is generated between the nozzle and a recessed tungsten electrode; the arc (ionized Ar) is then constricted or transferred to the substrate through a secondary gas system and a special nozzle design. Micro-plasma AM was conducted using an automated welding machine that provides a heat source with fully controllable voltage and amperage ranges, in addition to Automatic Voltage Control (AVC) for exact stand-off distance. The torch is controllable in the X, Y and Z axes and the wire feeder is speed controlled. Thermal management of the weld is achieved by pulsing the weld current and pulsing the weld wire into the developing weld pool.

The welding/printing setup for Inconel 718 involved a liquid cooled copper vice that held a sacrificial substrate in a vertical orientation. The plasma arc welding torch was placed vertically towards the vice, presenting a ‘down-hand’ welding position. The vice was held in a constant position for all specimens with marked lines on it to denote where the specimen sat within it. Both longitudinal and transverse specimens were fabricated with the same orientation. The equipment set up can be seen in Figure 19.

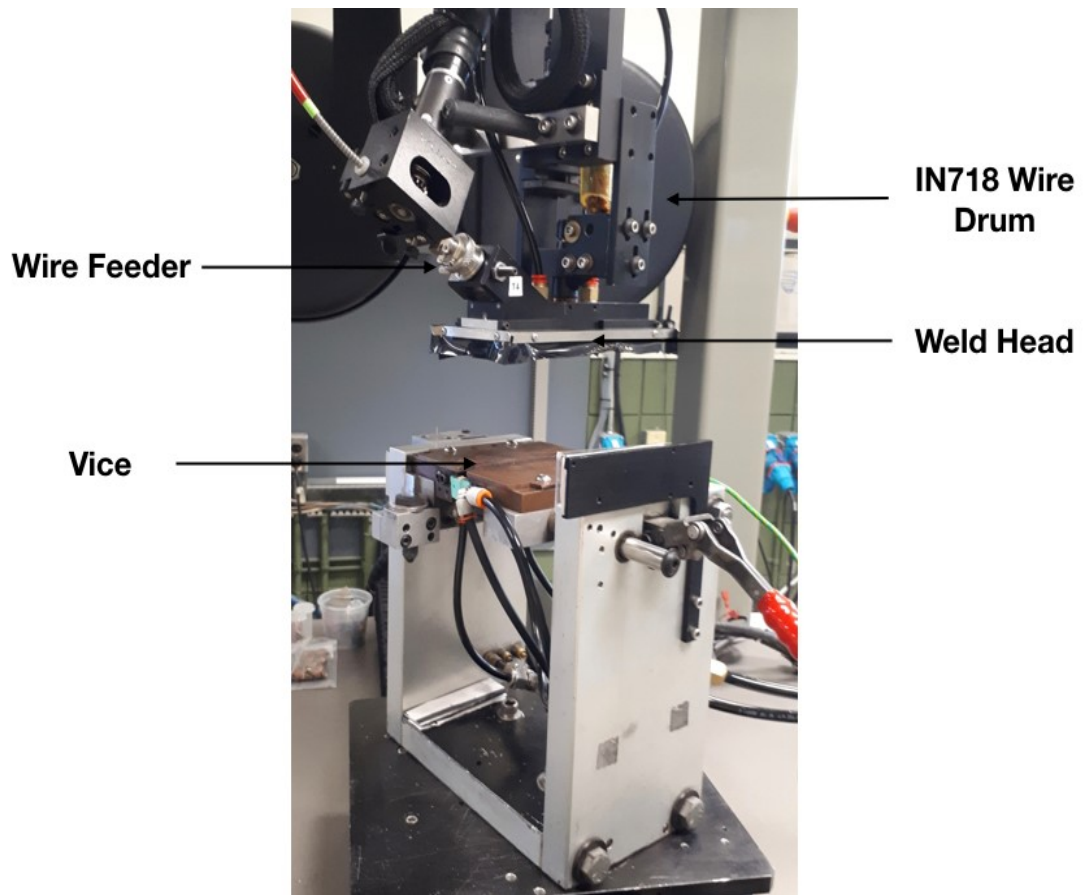


Figure 19. Additive manufacturing process setup

The Inconel 718 AM specimens were produced at open atmosphere with inert gas shielding and the first root pass for all the specimens had the same parameters. To start each specimen the LAWS500 machine was homed and zeroed. The machine has 4 axes (X, Y, Z and W),

but the W axis was not used in this study (torch rotation) and instead was kept in line with the vice. The wire feeder was positioned to feed directly into the advancing front of the weld pool. A simple rectangular shape was programmed using the parameters summarized in Table 5. The machine was recalibrated after every 4 specimens to avoid bead stacking faults arising from machine bias. Once all the required specimens were printed, they were heat treated to 1066°C for 2 hours and allowed to air cool to room temperature.

Table 5. Additive Manufacturing Process Parameters

High Current (A)	19.0/23
Low Current (A)	13.0/12
Pulse	3 Hz
Voltage (V)	19.6/19
Travel Speed (ipm)	3
High Wire Feed Rate (ipm)	33
Low Wire Feed Value	0.035s
Gas Used	H ₂ /95%Ar
Shield Gas Flow Rate (lpm)	13.5
Trail Gas Flow Rate (lpm)	30
Backup Gas Flow Rate (lpm)	4.5
Sample dimensions, mm x mm	Sample size 105mm x 20mm
Total process time (L/T min)	96/71

3.3 Inconel 718 specimen preparation

AM Inconel 718 specimens were milled, with a vertical milling attachment, to create a smooth surface for oxidation testing (as seen in Figure 20). Machining was done using a cobalt 4 flute center cut end mill with a shank diameter of $\frac{3}{8}$ " and at low speed to avoid heat generation.



Figure 20. Milling of AM Inconel 718 using a Sajo vertical milling attachment

Once all faces were milled, a Computer Numerical Control (CNC) machine was used to cut identical pieces. Approximately 3 flat end mills with a 0.045 in. diameter and a constant feed rate was used. Coolant was supplied constantly to prevent any heating while cutting the specimens. A CNC machine was also employed for cutting pieces off the wrought Inconel 718 (Figure 21).

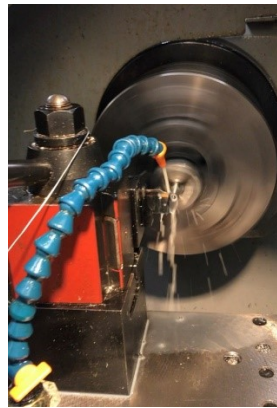


Figure 21. Milling of baseline wrought Inconel 718 using CNC milling

The final dimensions can be seen in Figure 22.

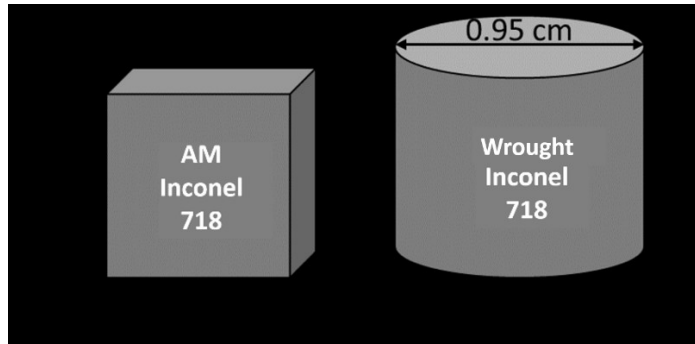


Figure 22. Measurements of AM (a) and baseline wrought (b) Inconel 718

Before oxidation, specimens were first polished using 120, 240, 400, and 600 grit SiC abrasive papers, and then cleaned ultrasonically in alkaline solution, water, and acetone separately, for 15 minutes in each condition. Trace humidity was eliminated by drying the specimens in a Cole-Parmer muffle furnace for two hours at 200°C, final specimens are shown in Figure 23. The specimens were then weighed in a Mettler Toledo AG285 scale (of 10^{-5} g precision). Clean handling gloves and individual storage bags were used for each specimen at all times to prevent the contamination of the specimens.

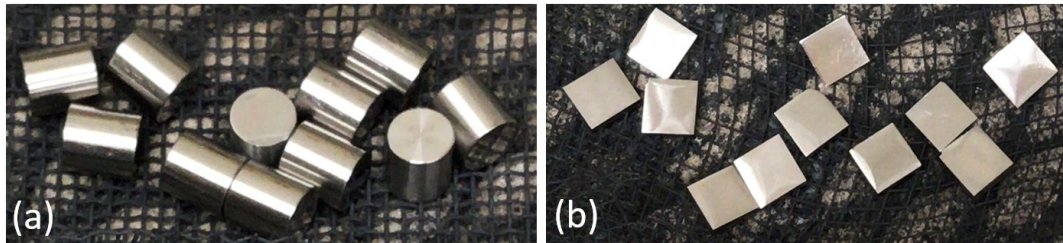


Figure 23. Baseline wrought (a) and AM (b) Inconel 718 specimens after removal of excess moisture

3.4 Inconel 718 specimen oxidation

To investigate the effect of different temperature and duration on the microstructure AM and wrought materials, a series of heat treatments were performed (summarized in Table 6). Specimens were oxidized in a Cole-Parmer muffle furnace at 800°C and 900°C for varying periods of time; note that temperature may vary by as much as 10°C to 15°C due to the capability of the air furnace. The selection of the two set temperatures are based on the maximum operating temperatures expected of this alloy.

Table 6. Oxidation Experiments with AM and baseline wrought Inconel 718

Alloy	Temperature (°C)	Oxidation Times (h)
AM Inconel 718	Ambient	0
	800	100, 200, 400
	900	50, 100, 200
Baseline wrought Inconel 718	Ambient	0
	800	100, 200, 400
	900	50, 100, 200

Three baseline and three AM specimens (on their respective crucibles) were placed within the oven at the start of each heat treatment. A specimen of each was removed at the predetermined time (50, 100, 200 or 400 hours as per Table 6).

Upon removal from the oven, specimens were air cooled until safe handling. Figure 24 shows the specimens after removal from the furnace.



Figure 24. Baseline wrought specimens after heat treatment at 800°C for 100, 200 and 400h, respectively

3.5 SEM and EDS specimen preparation

After oxidation, specimens were prepared for Scanning Electron Microscopy (SEM) and Energy-Dispersive Spectroscopy (EDS) analysis. In order to achieve high quality SEM images, metal (i.e. gold or copper) coating of the entire specimen is important; the metal coating improves the electron conductivity of the specimen and provides a protective coating in the oxidized specimens. A Quorum Q150T ES Specimen Preparation System was used, operating at 50A of current for 1-2 minutes of evaporation with a resulting 10-20 nm thick gold/copper layer. For specimens that were used for surface analysis, no coating or mounting were required.

After coating, the pucks were formed by fully covering them in bakelite resin. This was achieved by using a Buehler Simplemet II hydraulic press machine (Figure 25.a) operating at 9 psi for 15 minutes. Specimens were placed in such a way that the cross-sectional views of the specimen were facing upwards after retrieving. A total of 7 pucks were made, each puck included two specimen of AM Inconel 718 and the wrought specimen that was subjected to the same oxidation conditions.



Figure 25. Puck specimen preparation: (a) hydraulic press of Inconel 718 specimen with epoxy resin, (b) non-conditioned puck specimen, (c) auto polish of a puck and (d) conditioned puck specimen with mirror finish

The resulting pucks were then polished using a Buehler Auto Polisher (180 and 240 SiC, 9 μ m and 3 μ m diamond suspension, finished with 0.05 μ m alumina suspension) until mirror finish was achieved (i.e. surface does not have any visible scratches or other imperfections); Figure 25 shows a representation of the different steps.

The specimens that were not subjected to the oxidation were swabbed using Kalling's etchant in order to bring out the grain boundary structure (small changes in etching time can result in differences in the revealed microstructure). The Kalling's reagent is made of 1.5 g CuCl₂, 33 ml Ethanol, 33 ml distilled water and 33 ml HCl.

3.6 SEM and EDS analysis

The topography, morphology and composition of the resulting microstructures were analyzed at high vacuum in a Tescan VegaII XMU-SEM electron microscope which is equipped with Oxford X-ray detection systems (INCA EDS), as shown in Figure 26. Scanning electron microscopes (SEM) yield images with higher magnification, better resolution, and a larger depth of field than conventional optical microscopes.

This particular SEM has four-lenses, a resolution of 10 nm, a maximum magnification of 500 kx and a maximum accelerating voltage from 0.2 kV to 30 kV. The vacuum is generated by a turbomolecular and rotary force vacuum pump. It uses electrons from a tungsten filament for the imaging, the result is a surface profile for the specimen depicted as a 3D image. The Energy-Dispersive Spectroscopy (EDS) system is a semi-quantitative analysis method with a $\pm 2.5\%$ error margin. EDS is based on an x-ray detector, a liquid nitrogen chamber for cooling, and software to collect and analyze energy spectra. The detector is mounted in the specimen chamber of the main SEM.



Figure 26. Image of SEM and EDS

In order to analyze the specimens, carbon and copper are added to each puck; where carbon is a conductor and copper is the reference material used for equipment calibration. The pucks are first coated with conductive carbon using the same technique and equipment that was used for depositing gold or copper. A copper tape is added atop the carbon coat immediately prior to testing in the SEM machine. It is important to note that the different microstructural phases were identified by matching the EDS result to documented

compositions and morphologies seen in the literature; each region of interest was tested at least 7 times. The 7 resulting tests were then analyzed and used to identify composition and morphology trends that were then matched to literature. In the case where microstructures were complex and contained many phases in fine morphologies, it is possible that there are phases or structures that were simply too small to be seen with a SEM.

Chapter 4: Experimental Results and Discussion

Inconel 718 is a precipitation strengthened nickel (and iron) -based superalloy with refractory elements including niobium and molybdenum, in a nickel-chromium-iron matrix. The isothermal oxidation behavior of additive manufactured Inconel 718 and conventional baseline wrought Inconel 718 is reported this chapter. The objective of this chapter is to summarize the results that were obtained for the seven conditions of each material presented in Table 6 and compare the results among the two sets of specimens to those in the literature.

4.1 As-received and as-printed microstructures

An as-printed AM Inconel 718 specimen after polish and etching can be seen in Figure 27. No clear grain boundaries can be observed in the microstructure but some voids, likely remnants from the polishing, are still present (e.g. point 1). There are bright, elongated precipitates that can be identified as laves phase (point 2). The Laves phase has an A_2B formula composition, with Fe, Ni, and Cr in the A position and Nb, Mo, and Si in the B position (refer to Table 7). Laves phases are commonly present in cast alloy 718 as a consequence of elemental segregation of the Nb (and Mo) during the solidification; where the phase depicted in Figure 27 is a good example of their characteristic irregular shapes in inter-dendritic regions. When being exposed to high temperatures for a long period of time it typically resembles irregularly shaped globules or elongated platelets. A Laves phase is a brittle intermetallic phase formed when the Nb concentration exceeds 12 wt.% [63]. The Laves phase adversely influences the tensile ductility [64].

In addition to the presence of Laves phases, small spherical Ni-rich precipitates can be observed, likely Ni_3Nb (point 3). The compositions of the different phases of interest are presented as weight percentage and atomic percentage in Table 7.

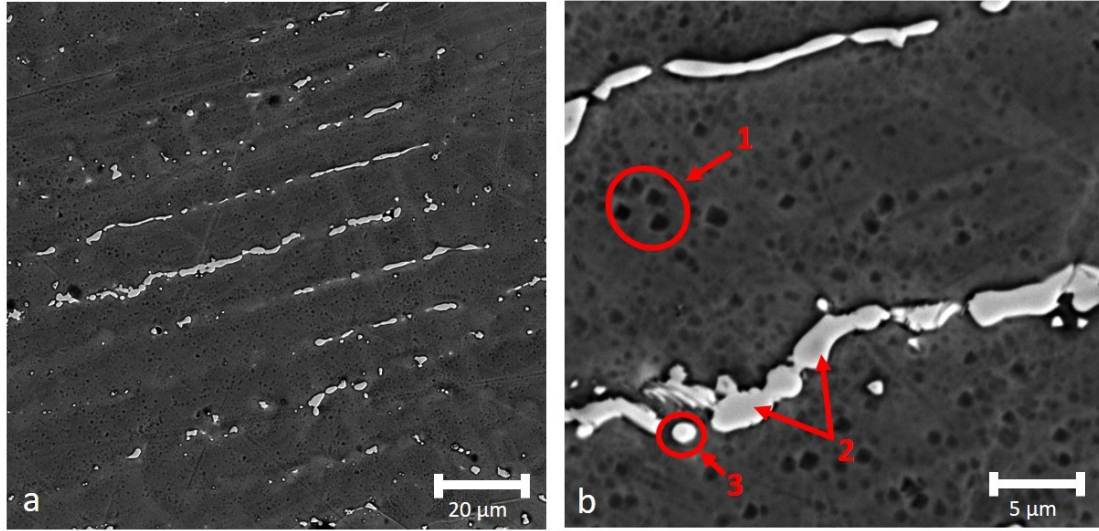


Figure 27. SEM image of as-printed AM Inconel 718 microstructure using a BSE detector with (a) 1000x and (b) 5000x magnification

Table 7. As-printed AM Inconel 718 composition

Weight %						
Points	Al	Ti	Cr	Fe	Ni	Nb
1. Matrix	1.00	0.82	20.24	21.18	54.41	2.35
2. Laves		1.02	13.61	13.02	38.76	33.58
3. Ni-rich precipitate		1.51	15.53	14.53	50.84	17.59
Atomic %						
Points	Al	Ti	Cr	Fe	Ni	Nb
1. Matrix	2.10	0.96	21.93	21.37	52.22	1.42
2. Laves		1.38	17.02	15.16	42.93	23.50
3. Ni-rich precipitate		1.91	18.15	15.81	52.63	11.51

Additive manufacturing is essentially a highly localized solidification process where the resulting microstructure is governed by heat transfer, solidification and phase

transformations [65]. Studies have concluded that in a powder bed AM process an increase in the spot size and power density resulted in increased solidification time and reduced temperature gradients, thus favoring the formation of equiaxed grain formation [66]. In this study, as shown in Figure 28, although the grain boundaries are not clearly seen, the usual dendritic structure of a cast is not observed.

Baseline wrought Inconel 718 presents more defined grain boundaries and an equiaxed grain structure (Figure 28), as opposed to the AM printed specimen. A similar microstructure was also observed by Rickenbacher et al. [67] on nickel-based superalloy Inconel 738. The matrix (point 1 in Figure 28) is a γ -FCC Ni-rich phase. Thin needles (δ -phase) are also visible inside equiaxed grains and along the grain boundaries (point 2 in Figure 28). Mo was not detected by SEM, this could be due to the overlap in the electron energy between Mo and Nb, making it difficult to differentiate the two elements (Table 8).

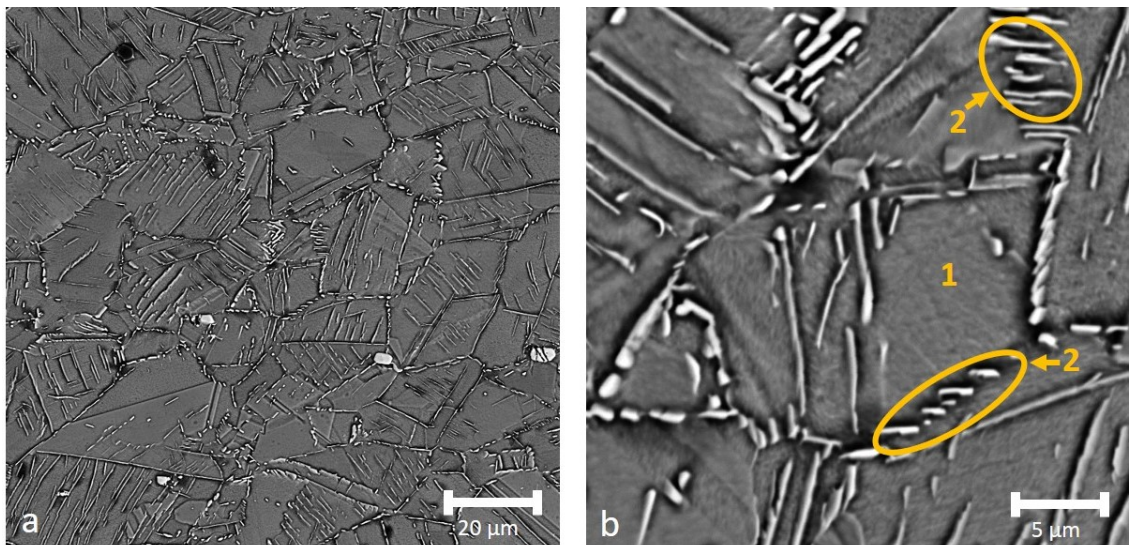


Figure 28. SEM image of as-received baseline wrought Inconel 718 obtained using a BSE detector at (a) 1000x and (b) 5000x magnification

Table 8. As-received baseline wrought Inconel 718 composition

Weight %						
Points	Al	Ti	Cr	Fe	Ni	Nb
1. Matrix	0.65	1.10	19.59	18.55	56.13	3.99
2. δ -Ni ₃ Nb	0.81	1.23	17.32	16.06	56.04	8.54
Atomic %						
Points	Al	Ti	Cr	Fe	Ni	Nb
1. Matrix	1.36	1.30	21.47	18.93	54.49	2.45
2. δ -Ni ₃ Nb	1.74	1.49	19.33	16.69	55.41	5.34

4.2 Weight change after oxidation

Weight gain was measured prior to oxidation test and at the different oxidation temperatures and times. To improve accuracy, the weight of each specimen was taken three times and then averaged. Table 9 and Table 10 summarize the weight change (and standard deviation) of the additively manufactured and baseline wrought Inconel 718 specimens respectively—Note that only the averaged final weights (before and after heat treatment) were used for the weight change per unit surface area over time.

Table 9. Weight change of AM Inconel 718 specimens

Additive manufactured Inconel 718								
		Before oxidation			After oxidation			
Temperature	Time (h)	Avg. weight sample (mg)	Standard deviation (mg)	Area (cm ²)	Avg. weight sample (mg)	Standard deviation (mg)	Δm (mg)	Weight change per unit area (mg/cm ²)
800°C	100	1072.733	0.047	1.980	1072.900	0.082	0.167	0.084
	200	1226.500	0	2.162	1226.867	0.047	0.367	0.170
	400	1143.667	0.047	2.049	1144.133	0.047	0.467	0.228
900°C	50	1037.733	0.047	1.971	1038.433	0.047	0.700	0.355
	100	1073.267	0.047	1.962	1074.267	0.047	1.000	0.510
	200	1086.967	0.047	1.960	1088.300	0.082	1.333	0.680

Table 10. Weight change of baseline wrought Inconel 718 specimens

Baseline wrought Inconel 718								
		Before oxidation			After oxidation			
Temperature	Time (h)	Avg. weight sample (mg)	Standard deviation (mg)	Area (cm ²)	Avg. weight sample (mg)	Standard deviation (mg)	Δm (mg)	Weight change per unit area (mg/cm ²)
800°C	100	5914.967	0.047	4.500	5915.333	0.047	0.367	0.0815
	200	6142.300	0	4.614	6142.967	0.047	0.667	0.1445
	400	6165.067	0.170	4.592	6166.133	0.047	1.067	0.2323
900°C	50	5745.933	0.047	4.458	5747.700	0	1.767	0.3963
	100	5940.167	0.047	4.469	5942.600	0.082	2.433	0.5444
	200	5929.500	0.082	4.454	5932.267	0.047	2.767	0.6212

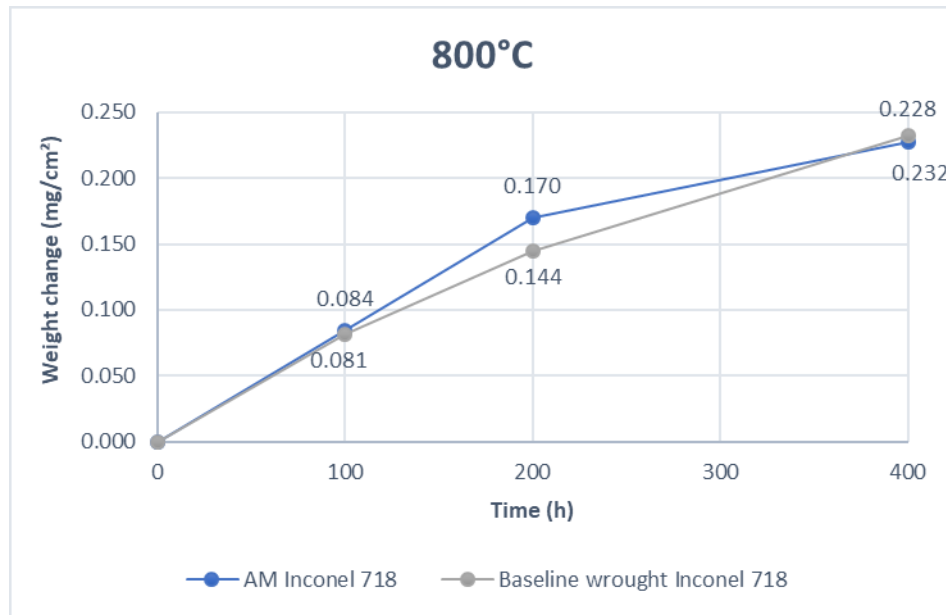


Figure 29. Weight change of Inconel 718 specimens at 800°C

At 800°C (Figure 29), AM and baseline wrought specimens show similar weight changes at 100h and 400h. Despite that the AM specimen showed a slightly higher weight change at 200h than the baseline wrought, the general trend highlights that the oxidation behaviour of AM and baseline wrought Inconel 718 is very similar. Greene et al. [68] reported that at

temperatures below 900°C, Inconel 718 experiences a period of transient oxidation after 24 hr of oxidation in air.

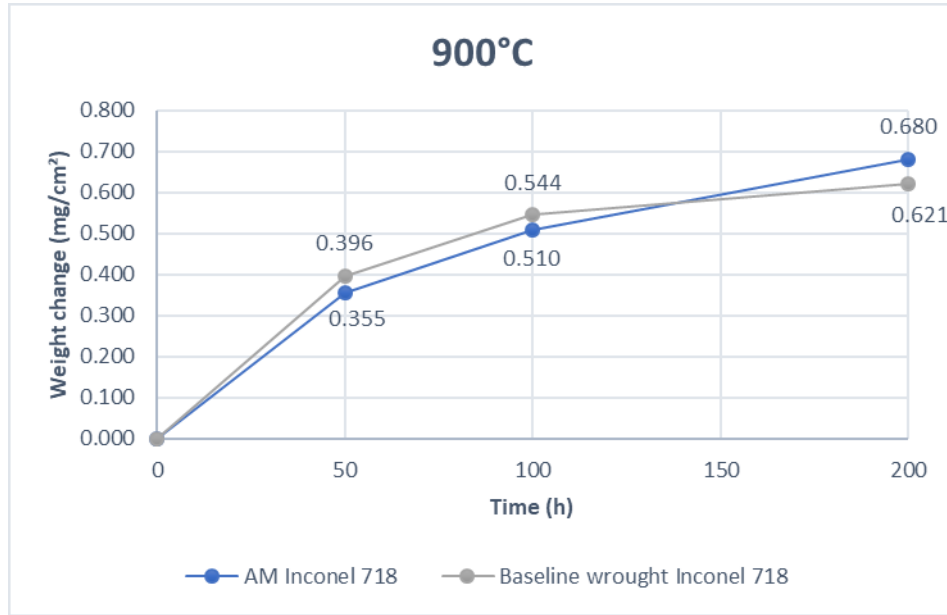


Figure 30. Weight change of Inconel 718 specimens at 900°C

At 900°C (Figure 30), there is a slightly more noticeable distinction between AM and baseline wrought Inconel 718. AM specimens had smaller weight gains after 50h and 100h, which implies that the specimens may have less oxidation for the first 100 hours and 200 h. At 200h, the weight gain surpasses the baseline wrought, possibility due to scale spallation on the baseline wrought 718. It's important to emphasize that oxidation treatment at 800°C had favorable outcomes, showing lesser weight gain over time thanks to the formation of chromia oxide layer. With an increase in temperature by 100°C there is a three-fold increase in weight gain for both AM and baseline wrought specimens. This is due to the increasing driving force for oxidation with higher temperature.

Furthermore, the square of the mass gain per unit area is shown in Figures 31 and 32 where mass gain per unit area increases linearly with increasing time. A curve fit yields the parabolic oxidation rate constant (K_p). The value of K_p validates the prior findings, i.e., at 900°C a higher oxidation rate is observed in both specimens and also higher oxidation rate is perceived for AM Inconel 718 at both temperatures, although the difference is minimal at 800°C.

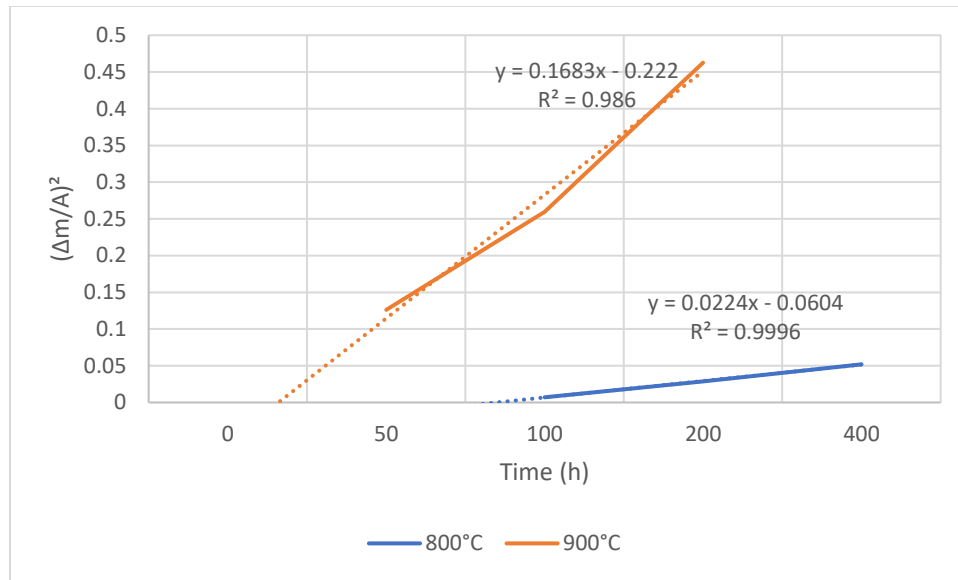


Figure 31. Square of the mass gain per unit area versus time for AM Inconel 718 oxidized in air at temperatures at 800°C and 900°C for up to 400hr

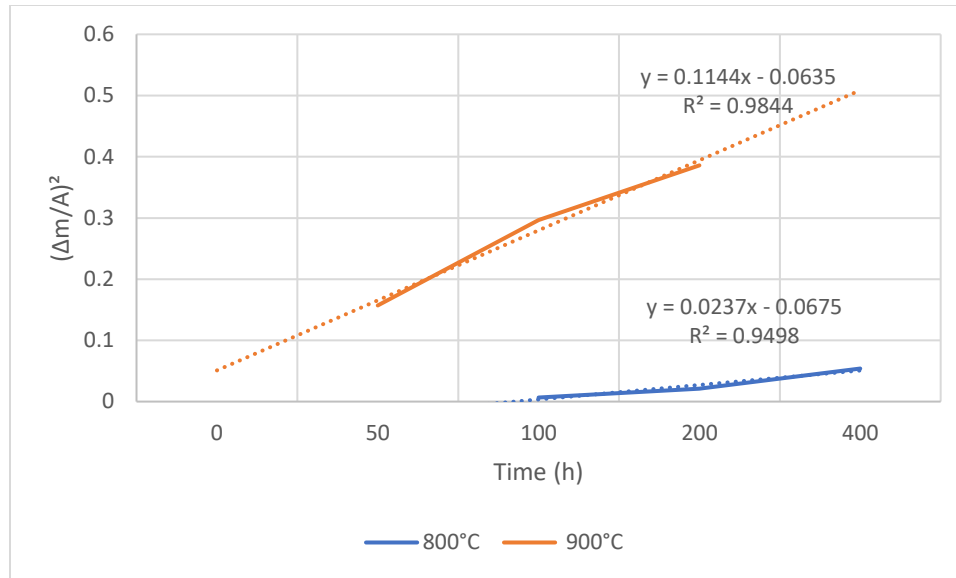


Figure 32. Square of the mass gain per unit area versus time for baseline wrought Inconel 718 oxidized in air at temperatures at 800°C and 900°C for up to 400hr

4.3 Surface oxide formation and oxidation behavior at 800°C

The isothermal oxidation behavior of additive manufactured Inconel 718 and conventional baseline wrought Inconel 718 at 800°C is presented in this section. Note that using the EDS analysis method, it is not possible to delineate exactly which oxide is formed, as such Cr-rich or Ni-rich oxide is used to describe the oxides formed in different regions throughout this research.

4.3.1 Surface oxides

The surface microstructure of the different specimens at different oxidation duration is presented here. The expectation was for chromia oxide layers to form on the surface, given the composition of Inconel is enrich in Cr; indeed, chromia oxides are present on both AM

and baseline wrought Inconel 718, Figure 33. The external oxide scale is homogenous and adherent.

It is hard to quantify the thickness changes of Cr_2O_3 as a function of time, but the obvious changes in oxide shape and size are noted where longer exposures result in larger chromia precipitates as can be seen in Table 11.

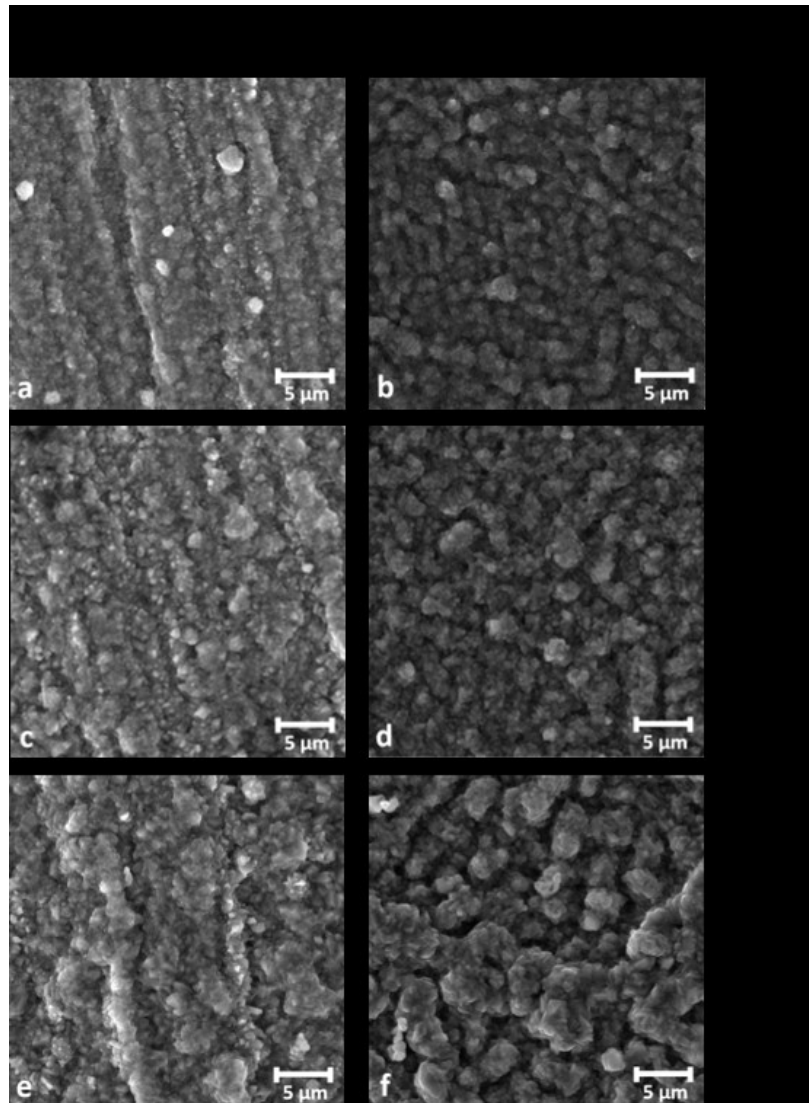


Figure 33. Surface oxide topography of AM and baseline wrought Inconel 718 specimens oxidized at 800°C for different times ranges.

Table 11. EDS composition of surface oxide at 800°C

Weight %								
Specimen	O	Al	Ti	Cr	Mn	Fe	Ni	Nb
a	29.15	0.48	3.98	54.82	2.20	1.80	6.30	1.26
b	33.01		2.79	44.24		4.57	13.07	2.32
c	29.63	0.41	2.54	47.81	1.81	3.30	12.12	2.37
d	35.82		2.12	44.13		1.56	3.88	12.50
e	35.62		5.01	53.83	3.25	0.56	1.36	0.38
f	32.54		2.24	59.85		1.02	3.47	0.88
Atomic %								
Specimen	O	Al	Ti	Cr	Mn	Fe	Ni	Nb
a	57.46	0.56	2.62	33.26	1.26	1.02	3.39	0.43
b	62.49		1.76	25.77		2.48	6.74	0.76
c	58.54	0.48	1.68	29.06	1.04	1.87	6.52	0.81
d	66.63		1.32	25.26		0.83	1.97	4.00
e	64.30		3.02	29.90	1.71	0.29	0.67	0.12
f	61.29		1.41	34.69		0.55	1.78	0.29

4.3.2 Inconel 718 substrate microstructural changes after 800°C oxidation test

The substrate microstructure changes are viewed on the cross-sections of specimens after oxidation. Figure 34 highlights the microstructural changes of both AM and baseline wrought Inconel 718 after being oxidized at 800°C for different time intervals. Figure 34.a and Figure 34.b represent the as-printed and as-received microstructures that were already presented in the previous section.

A total of three key phases were identified for both AM and baseline wrought Inconel 718. The key differences between both specimens are: the size of the delta phase, the grain boundary precipitates, and also the occurrence and distribution of γ' . Table 12 and Table 13 summarize the EDS analysis results of different phases in both alloys oxidized for three different durations.

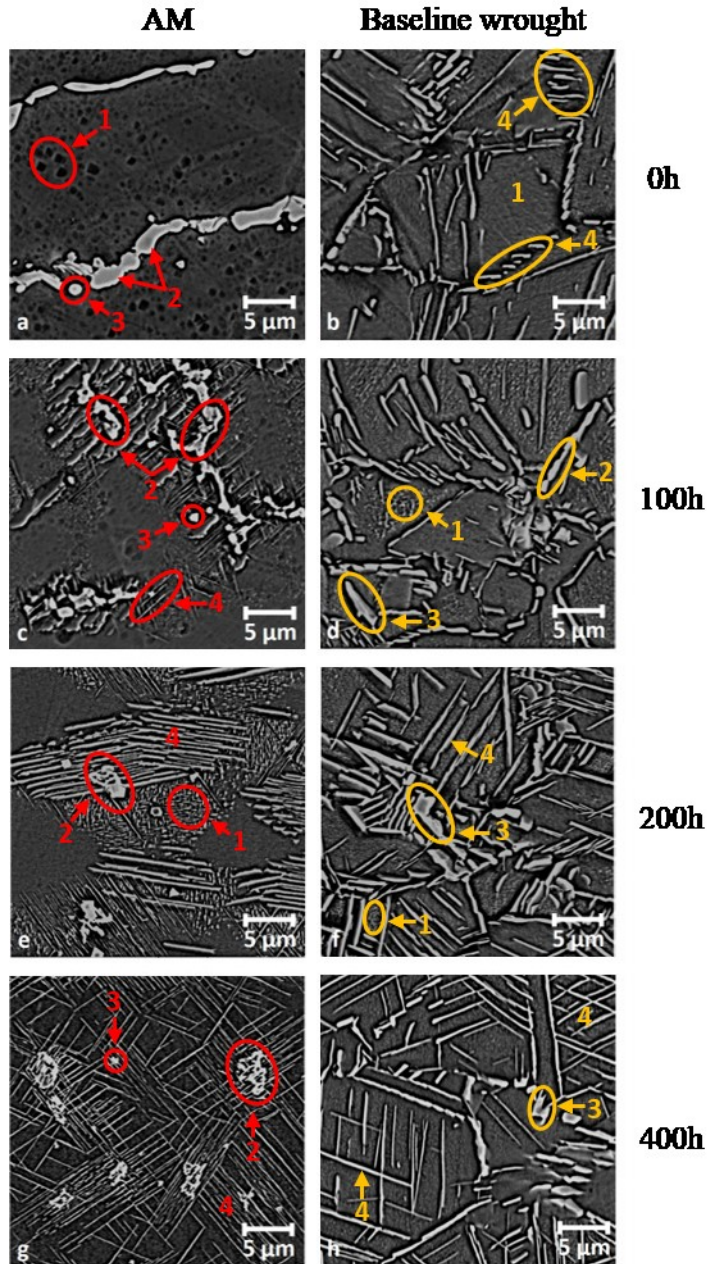


Figure 34. Microstructure of AM and baseline wrought Inconel 718 specimens oxidized at 800°C for different times.

The first phase of interest (point 1 in Figure 34) is the matrix of the AM Inconel 718 metal, which has small spherical γ'' precipitates. This matrix is similar to baseline wrought

specimen given the composition resemblance of the original two alloys (e.g. Figure 34.d and Figure 34.e).

Table 12. Composition analysis for AM Inconel 718 specimens held at 800°C

Weight %						
Points	Al	Ti	Cr	Fe	Ni	Nb
1. Matrix	0.92	1.20	19.24	19.25	55.03	4.35
2. Laves		1.79	15.34	8.53	46.97	27.37
3. Ni-rich precipitate		1.51	15.53	14.53	50.84	17.59
4. δ-Ni₃Nb		1.16	18.91	18.55	54.70	6.68
Atomic %						
Points	Al	Ti	Cr	Fe	Ni	Nb
1. Matrix	1.94	1.43	21.05	19.61	53.31	2.66
2. Laves		2.37	18.67	9.67	50.64	18.65
3. Ni-rich precipitate		1.91	18.15	15.81	52.63	11.51
4. δ-Ni₃Nb		1.40	21.10	19.27	54.06	4.17

Laves phases, point 2 in Figure 34, is a detrimental solidification phase in Inconel 718 that can present itself in both welded (AM is essentially a multiple pass welding process) and cast products when alloying elements Nb, Mo, Ti, and Si exceed their solubility limit in the austenite matrix [64]. Laves phase formation also depends on the initial grain structure and composition of the base metal [69]; the proper selection of alloying elements in Inconel 718 can help minimize its formation [70]. With given alloy compositions and manufacturing methods used in this study, the morphology of the Laves phases changes with time, from globular (Figure 34.a) to more blocky (Figure 34.f) and finally irregularly shaped (Figure 34.g). High temperature and extended exposures promote the formation of Laves phase.

Table 13. Composition analysis for baseline wrought Inconel 718 specimens held at 800°C

Weight %						
Points	Al	Ti	Cr	Fe	Ni	Nb
1. Matrix	0.65	0.96	17.35	16.04	56.30	8.70
2. Laves		2.15	4.67	5.05	60.36	27.76
3. γ''-Ni₃Nb		1.62	11.36	10.29	57.10	19.63
4. δ-Ni₃Nb		1.45	14.28	12.77	58.64	12.85
Atomic %						
Points	Al	Ti	Cr	Fe	Ni	Nb
1. Matrix	1.41	1.16	19.43	16.72	55.83	5.45
2. Laves		2.90	5.79	5.83	66.24	19.25
3. γ''-Ni₃Nb		2.09	13.49	11.37	60.02	13.04
4. δ-Ni₃Nb		1.81	16.44	13.69	59.78	8.28

The presence of δ -Ni₃Nb is seen in both AM and baseline wrought Inconel 718 (needle shape as shown in point 4 in Figure 34). It has similar composition as γ'' phase which is responsible for the elevated temperature strength of the material. The main difference between these phases is their morphology as δ phase is characterized as being needle as shown in Figure 34.b while γ'' assumes spherical or cuboidal shape. Delta phase generally precipitates on grain boundaries by nucleation followed by the growth of thin plates (needles) extending into the grains, which retards grain size growth during thermal exposure [71]. It has been reported that the metastable γ'' phase can undergo a slow transformation into δ phase (point 4 Figure 34) if the operating temperature is >650°C [27] [72]. As the exposure time increases in AM and baseline wrought specimens (from 100h to 200h and finally to 400h) we first see an increase in γ'' phase until 200 hours and then at 400h a decrease is observed due to the transition into δ phase along the grain boundaries and within the matrix.

Other researchers have concluded that in Inconel 718 MC carbide (TiC or NbC) may be present [73], however given that the SEM specimens were coated with carbon for testing, it is hard to conclude if some of the blocky particles present on the grain boundary region are carbides. It is likely that the phases labelled by point 3 in both AM and baseline wrought specimens are carbide in nature due to their morphologies.

4.3.3 Cross-section of Inconel 718 after 100h of exposure

The AM specimen exhibited an oxide layer atop the metal surface, as can be seen in Figure 35. In this image, four different regions are observed, and EDS analysis is carried out on these regions to support the identification of the phase.

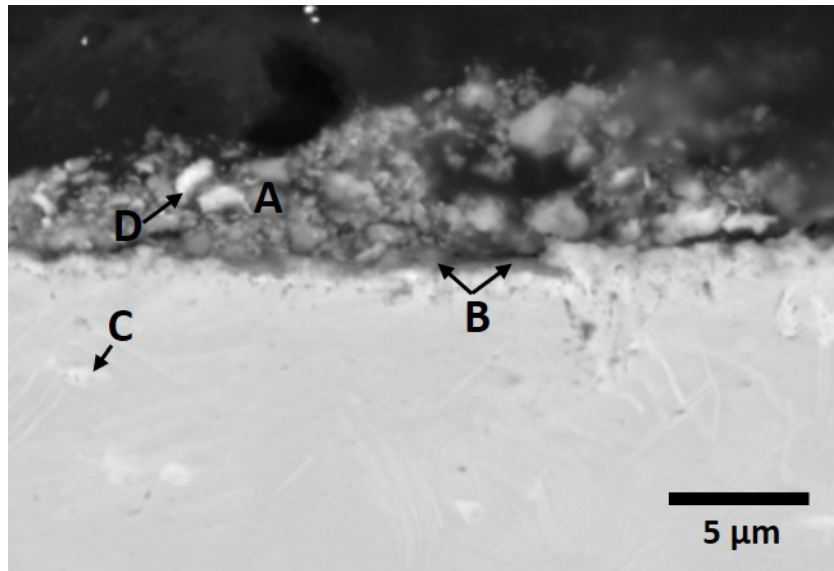


Figure 35. Oxide layers on AM Inconel 718 after 100h at 800°C

Table 14. Composition of AM Inconel 718 after 100h at 800°C

Element	Atomic %				Weight %			
	A	B	C	D	A	B	C	D
O K	52.48	12.33		31.74	25.52	4.02		11.80
Al K	1.13	1.34		2.12	0.93	0.73		1.33
Ti K	1.40	2.49	12.86	1.40	2.04	2.43	8.65	1.56
Cr K	42.66	49.87	12.56	22.98	67.41	52.78	9.17	27.76
Fe K	0.80	9.72	9.61	10.59	1.35	11.05	7.54	13.74
Ni K	1.54	24.25	43.86	29.53	2.75	28.98	17.41	40.28
Nb K			21.11	1.64			57.23	3.54

Region A consists mainly of Cr and O elements which can be inferred to be the chromia oxide layer (elemental composition given in Table 14). It is not possible to estimate the layer thickness as the chromia layer is very uneven. There are several bright particles in the Cr₂O₃ layer that are rich in Ni and Nb (region D). Between the oxide and substrate metal, there is occasional dark spots (region B) with elevated Ni and Fe, a possibility of NiO or FeO formation. Lastly, the presence of Laves phase is evident in region C, besides thin elongated δ plates.

Similar to the AM specimen, the baseline wrought specimen (Figure 36) also contains a Cr₂O₃ layer that is adherent (region A). However, comparing to AM specimen oxidized under the same condition, the Cr content detected on the top layer is much lower, due to the extremely thin submicron layer. Below the chromia layer, there is a thin Ni and possibly Nb-rich sublayer (region B) that covers the majority of the surface. In region C, further nearing the substrate, the oxide also appeared to be Ni rich; possibly an indication of gradual Cr depletion in the alloy, leading to NiO formation. Lastly, in region D, there is an enrichment of Nb, in comparison to the other regions; based on its composition it is determined to be a δ -Ni₃Nb phase (Table 15).

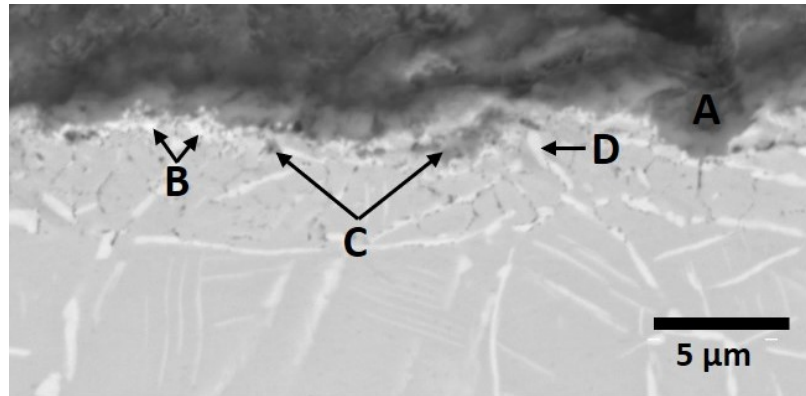


Figure 36. Oxide layers on the baseline wrought Inconel 718 after 100h at 800°C

Table 15. Composition of baseline wrought Inconel 718 after 100h at 800°C

Element	Atomic %				Weight %			
	A	B	C	D	A	B	C	D
O K	71.55	46.85	28.91	8.13	43.49	19.90	10.56	2.26
Al K	1.00	2.99	6.17	1.50	1.03	2.14	3.80	0.71
Ti K	1.86	1.54	3.57	1.65	3.38	1.96	3.90	1.37
Cr K	22.07	10.50	10.11	8.23	43.59	14.49	12.01	7.45
Fe K	0.76	8.66	12.99	11.62	1.62	12.84	16.57	11.30
Ni K	2.17	26.43	35.85	57.95	4.84	41.20	48.07	59.24
Nb K	0.58	3.03	2.40	10.92	2.05	7.47	5.09	17.66

4.3.4 Cross-section of Inconel 718 after 200h of exposure

After 200 hours of exposure at 800°C, AM Inconel 718 specimen reveals a more dense outer oxide layer (about 5 μm) than that observed after 100h of exposure (Figure 37, region A) where Ni is the major element instead of Cr, Table 16, pointing to a possible chromia depletion or chromia scale spallation. In region B, between the oxide and substrate, it seems that internal oxidation has progressed beneath the specimen's surface. Region B is rich in Ni and Fe. Laves phases are also present in this specimen surrounding thin δ needles further into the substrate (region C).

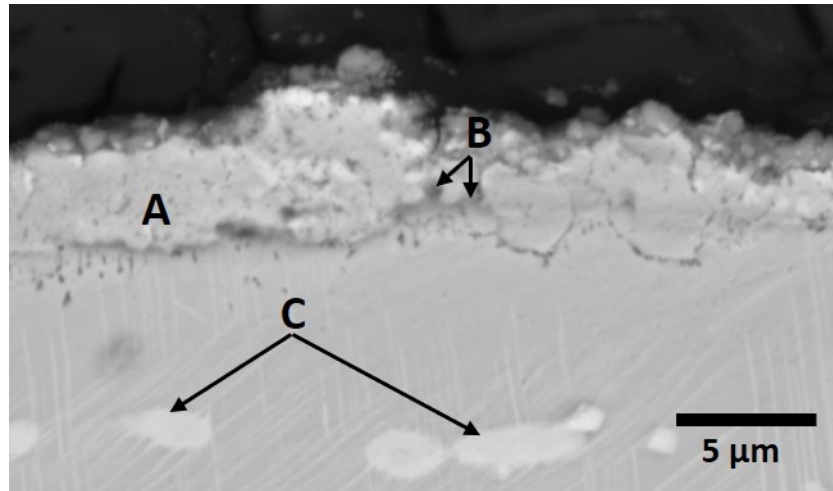


Figure 37. Oxide layers on AM Inconel 718 after a 200h at 800°C

Table 16. Composition of AM Inconel 718 after 200h at 800°C

Element	Atomic %			Weight %		
	A	B	C	A	B	C
O K	10.01	12.02		3.06	3.70	
Al K	1.46	1.52		0.75	0.79	
Ti K			1.24			0.92
Cr K	15.26	12.50	17.71	15.16	12.53	14.35
Fe K	20.96	20.77	16.91	22.36	22.35	14.72
Ni K	52.30	52.49	42.91	58.66	59.37	39.26
Nb K		0.70	21.23		1.25	30.75

The baseline wrought specimen continues to a compact but uneven Cr₂O₃ layer (Figure 38, region A) with peaks and valleys. It contains a greater Cr content than that formed on the AM specimen after 100h and 200h. Region B is a thinner layer composed of Nb and Ni rich compound/oxide (Table 17); this Nb rich layer may have contributed to the impeded Cr depletion observed on the baseline wrought specimens that were oxidized under the same conditions as AM specimens. Given that regions B and C have similar Nb content, indicating the formation of Ni₃Nb.

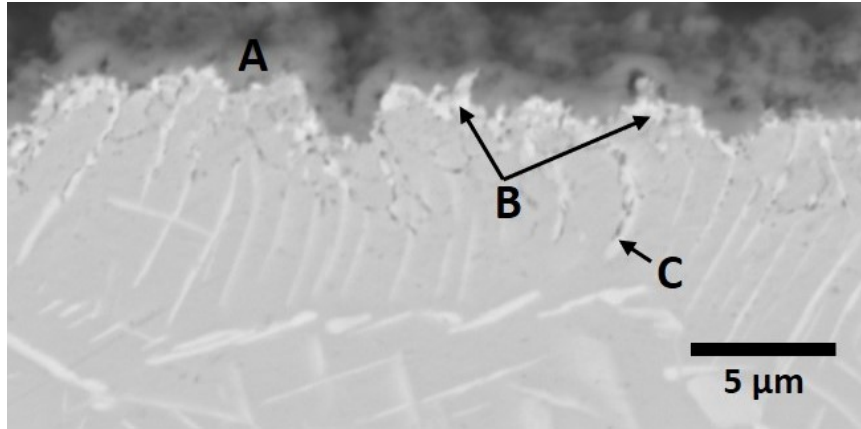


Figure 38. Oxide layers on the baseline wrought Inconel 718 oxide layers after 200h at 800°C

Table 17. Composition of baseline wrought Inconel 718 after 200h at 800°C

Element	Atomic %			Weight %		
	A	B	C	A	B	C
O K	61.02	39.81		31.55	14.57	
Al K	0.92	1.73		0.80	1.07	
Ti K	1.53	0.58	0.97	2.37	0.63	0.77
Cr K	24.01	7.41	13.00	40.35	8.81	11.20
Fe K	2.73	4.87	15.13	4.93	6.22	14.00
Ni K	8.51	36.03	61.99	16.14	48.36	60.31
Nb K	1.28	9.58	8.91	3.85	20.34	13.72

4.3.5 Cross-section of Inconel 718 after 400h of exposure

After 400 hours exposure at 800°C, both AM and baseline wrought Inconel 718 specimens (Figures 39 and 40) contain a clear Cr₂O₃ layer as their outer oxide layer (region A in both specimens). A Ni and Nb-rich thin sublayer in region B is considered to be Ni₃Nb based on the elemental composition shown in Table 18 and Table 19. This reoccurrence of Cr-rich oxide layer on AM Inconel 718 specimens may be attributed to Ni-rich oxide scale

spallation and the re-formation of Cr-rich oxide layers afterwards. Region C in both specimens are Ni rich with low Cr concentrations.

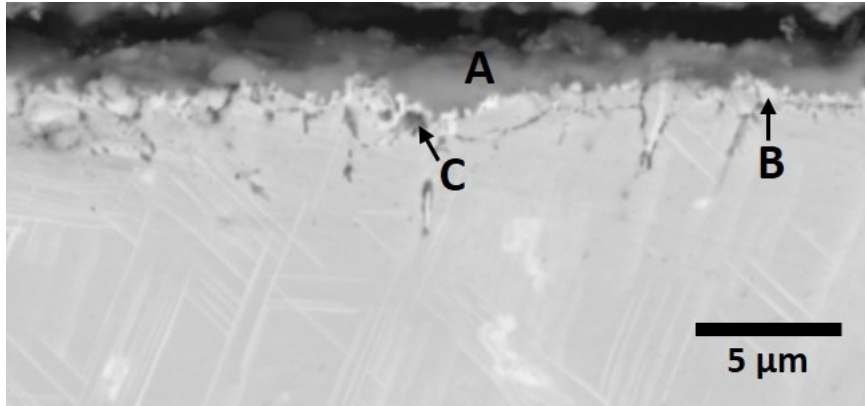


Figure 39. Oxide layers on AM Inconel 718 after 400h at 800°C

Table 18. Composition of AM Inconel 718 after 400h at 800°C

Element	Atomic %			Weight %		
	A	B	C	A	B	C
O K	71.01	60.97	42.29	43.35	29.59	17.17
Al K	1.15	1.68	3.85	1.19	1.37	2.64
Ti K	0.76	0.73	3.46	1.38	1.06	4.21
Cr K	25.46	10.16	11.03	50.52	16.03	14.56
Fe K	0.57	2.76	7.85	1.21	4.68	11.13
Ni K	1.05	18.80	27.68	2.35	33.47	41.24
Nb K		4.90	3.84		13.80	9.05

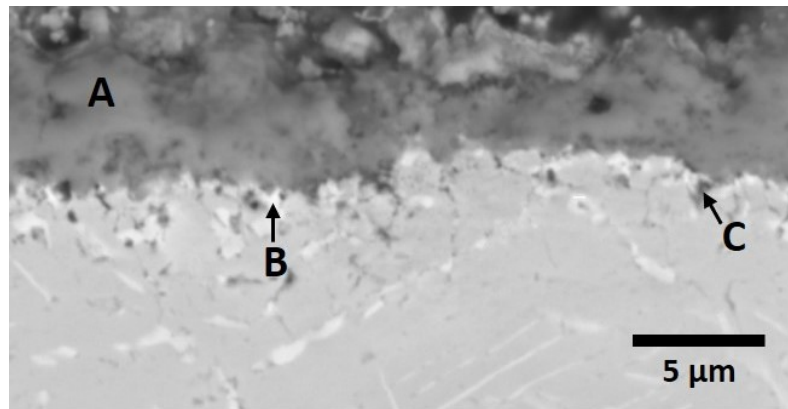


Figure 40. Oxide layers on the baseline wrought Inconel 718 after 400h at 800°C

Table 19. Composition of baseline wrought Inconel 718 after 400h at 800°C

Element	Atomic %			Weight %		
	A	B	C	A	B	C
O K	68.01	9.91	40.22	38.40	2.72	17.79
Al K	0.44	2.70	18.61	4.77	1.25	13.88
Ti K	0.63	1.28	0.44	0.84	1.05	0.58
Cr K	29.93	7.97	7.49	25.01	7.11	10.76
Fe K	0.42	9.37	8.66	5.86	8.97	13.37
Ni K	0.58	52.18	20.64	12.53	52.50	33.49
Nb K		16.58	3.94	12.59	26.40	10.11

Finally, to complement the cross-sectional analysis of the specimens oxidized at 400h, several elements were mapped with the resulting images shown in Figure 41. As shown in these maps, Cr and O are seen atop of the surface, representing the protective chromia layer. It is important to note that the Cr-oxide layer is much thinner for AM specimen, about 3-4 times thinner than that on the baseline wrought specimen. The Nb/Mo enrichment below Cr-oxide layer is more evident for the wrought alloy. Based on both SEM/EDS and X-Ray mappings, it is likely that baseline wrought Inconel 718 has a better oxidation resistance due to the formation of a thin Nb/Mo layer below the Cr-rich oxide and also thicker Chromia formation.

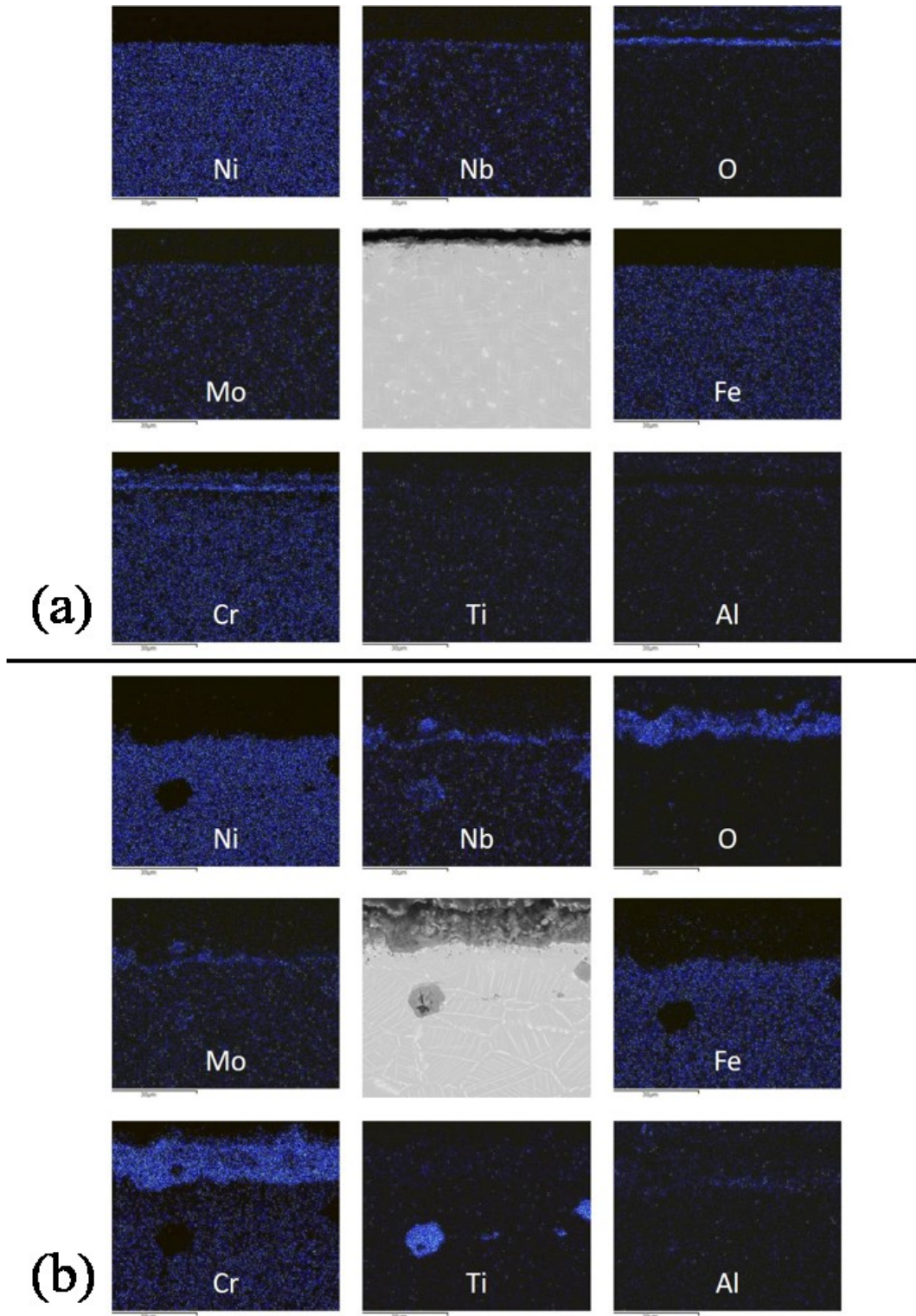


Figure 41. X-ray mapping of (a) AM and (b) Baseline wrought Inconel 718 after 400h at 800°C

4.4 Surface oxide formation and oxidation behavior at 900°C

The isothermal oxidation behavior of additive manufactured (AM) Inconel 718 and conventional baseline wrought Inconel 718 at 900°C is presented in this section.

4.4.1 Surface oxides

At 900°C, the expectation was for chromia oxide layers to form on the surface given that Inconel 718 is enriched in Cr. The formation of these chromia oxides was confirmed on both AM and baseline wrought Inconel 718 at 900°C and can be seen in Figure 42.

The oxide scale was found to be relatively compact and adhered to the surface of the AM specimen. As time progressed the fine surface oxide started to agglomerate from 50 to 200 hours (Figure 42). While we cannot quantify the thickness of chromia oxide layer, it is assumed that the oxide layer grew over time. The baseline wrought Inconel 718 does not show such a clear agglomeration, but the growth of the thickness of chromia layer with time can also be assumed (Table 20). Similar results were attained by Sanviemvongsak et al. [55] for the same material oxidized at 850°C in air for 1000hrs where they concluded that the chromia oxide layer formed was homogenous, adherent to the surface.

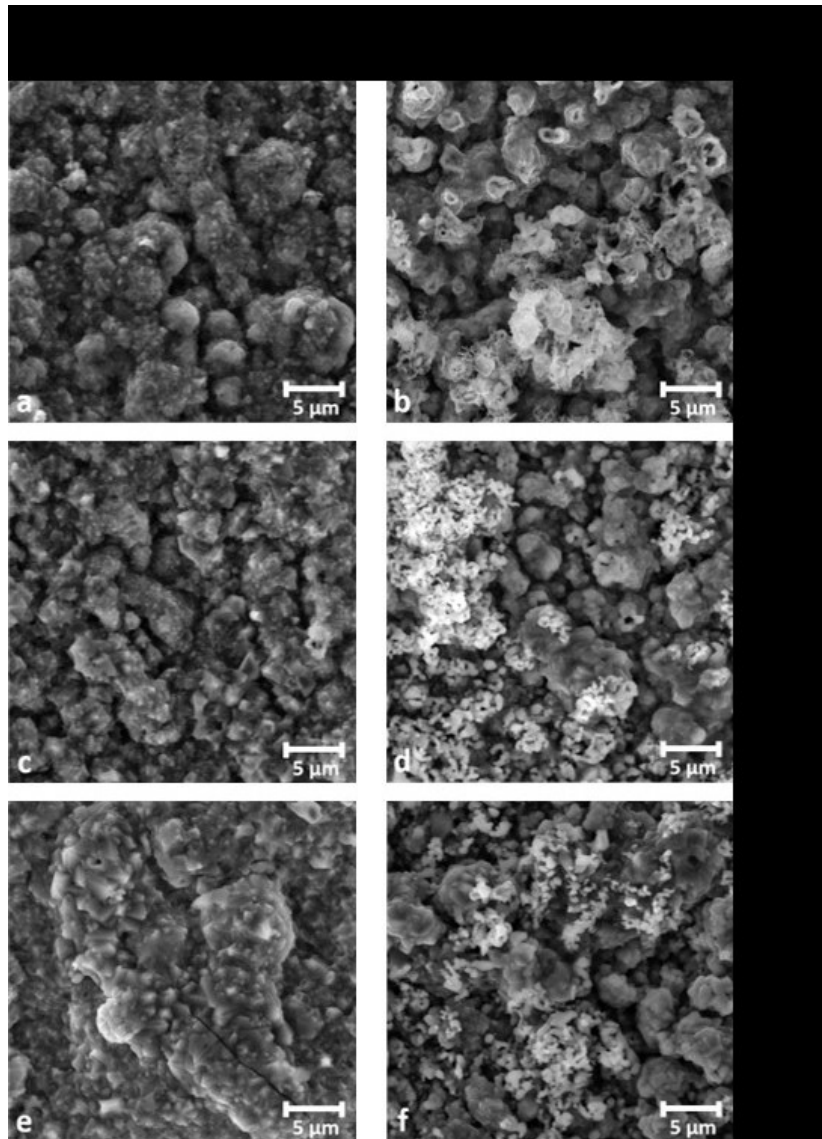


Figure 42. Surface oxide topography of AM and baseline wrought specimens Inconel 718 oxidized at 900°C for different times ranges.

Table 20. EDS composition of surface oxide at 900°C

Weight %								
Specimen	O	Al	Ti	Cr	Mn	Fe	Ni	Nb
a	32.52		2.48	58.69	3.69	0.83	1.30	0.49
b	34.47		2.50	57.34		1.43	2.34	1.92
c	31.04		1.47	59.53	3.43	1.29	2.29	0.96
d	32.21	0.27	1.62	56.12		2.74	2.84	4.19
e	35.60		1.43	52.84	7.94	0.69	1.02	0.48
f	29.94		5.64	59.50		1.19	2.92	0.82
Atomic %								
Specimen	O	Al	Ti	Cr	Mn	Fe	Ni	Nb
a	61.18		1.56	33.97	2.02	0.45	0.67	0.16
b	63.45		1.54	32.48		0.75	1.17	0.61
c	59.69		0.95	35.22	1.92	0.71	1.20	0.32
d	61.40	0.30	1.03	32.92		1.49	1.48	1.38
e	64.48		0.87	29.45	4.19	0.36	0.50	0.15
f	58.24		3.66	35.61		0.66	1.55	0.28

4.3.2 Base metal microstructure changes after 900°C oxidation test

The substrate microstructure changes were viewed on the cross-sections of specimens after oxidation, further from the surface. Figure 43 highlights the microstructural changes of both AM and baseline wrought Inconel 718 after being oxidized at 900°C. The same three main phases, γ'' , δ and Laves phase, are identified for both AM and baseline wrought Inconel 718 after oxidation at this temperature; however, some differences were identified by comparing the microstructure changes and the elemental compositions of interested phases as shown in Tables 21 and Table 22.

The first phase of interest (point 1 in Figure 43) is the base metal, which is the FCC Ni-rich matrix with small spherical γ'' precipitates. This matrix morphology is similar in both baseline wrought and AM specimens regardless of temperature due to comparable compositions.

The second phase is Laves phase. Laves phase is an intermetallic phase that is formed when the Nb (+Mo) concentration exceeds 12 wt.% [18]. The Laves phase is identified as point 2 in Figure 43 for both specimens. In the AM specimen, it was found in the vicinity of delta phases (point 4) and in the baseline wrought specimen it was only found as elongated and circular phases after a 200h (Figure 43.h). This is an important observation since Laves phase is considered a deleterious phase, reducing both material's ductility and fracture toughness. As the baseline wrought material is observed here to be more resistant to brittle phase formation during high temperature exposure, it is reasonable to assume that the AM material will require further microstructure modification in order to reduce the occurrence of Laves phase.

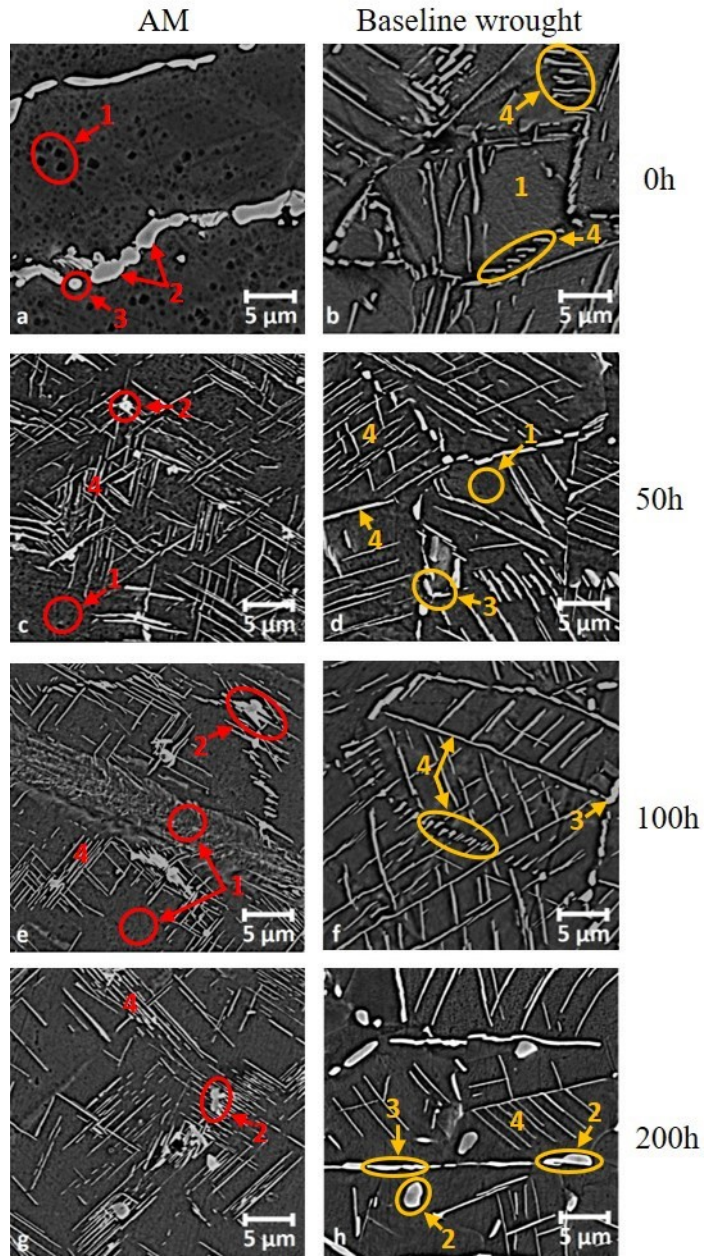


Figure 43. Microstructure of AM and baseline wrought Inconel 718 specimens oxidized at 900°C for different times ranges.

Thirdly, δ -Ni₃Nb continues to be present in both AM and baseline wrought Inconel 718 (needle shape as shown in point 4 in Figure 43). δ phase in Inconel 718 is useful for controlling grain size, particular if it precipitates along the grain boundaries [74]. Based on these images, there is not delta phase in the AM material under the as-printed condition; after the oxidation at 900°C, the amount of delta phase appears to be inversely proportional to time for the AM specimen (at 800°C there did not appear to be a correlation). For the baseline wrought specimens, delta phase is present under all conditions, however, there is an evidence of the plate size/thickness increase as the increase of duration. As discussed previously, delta phase generally precipitates on grain boundaries by nucleation and is followed by the growth of thin plates (needles); this is especially evident in the baseline wrought specimen. Although EDS results are only semi-quantitative and not accurate for small particles, it is possible the phases within the baseline wrought specimen, labelled as 2, are in fact coalesced delta phase. In addition, there is an abundance of delta phase found with the grains for both AM (oxidized) and baseline wrought specimens (all conditions). With increased temperature or exposure time, it is believed that these precipitates will start to dissolve into the matrix. This was confirmed by Tucho et al. [75] who used different temperatures and hold times to investigate the dissolution of Inconel 718 precipitates; they concluded that annealing at 1250°C resulted in the complete dissolution of precipitates located within and along the sub-grain boundaries.

Table 21. Composition analysis for AM Inconel 718 specimens held at 900°C

Weight %						
Points	Al	Ti	Cr	Fe	Ni	Nb
1. Matrix	0.70	0.86	20.74	21.45	54.22	2.02
2. Laves		2.28	10.85	10.84	50.89	25.14
3. Ni-rich precipitate		1.51	15.53	14.53	50.84	17.59
4. δ-Ni₃Nb		1.15	17.59	17.89	56.58	6.78
Atomic %						
Points	Al	Ti	Cr	Fe	Ni	Nb
1. Matrix	1.47	1.01	22.51	21.67	52.11	1.23
2. Laves		3.00	13.14	12.23	54.59	17.04
3. Ni-rich precipitate		1.91	18.15	15.81	52.63	11.51
4. δ-Ni₃Nb		1.40	19.68	18.63	56.05	4.24

Table 22. Composition analysis for baseline wrought Inconel 718 specimens held at 900°C

Weight %						
Points	Al	Ti	Cr	Fe	Ni	Nb
1. Matrix	1.04	0.83	20.97	20.16	55.07	1.93
2. Laves		2.79	4.20	4.47	61.25	27.31
3. Ni-rich precipitate		1.97	8.34	7.73	60.61	21.35
4. δ-Ni₃Nb	0.75	0.97	19.61	18.02	55.52	5.15
Atomic %						
Points	Al	Ti	Cr	Fe	Ni	Nb
1. Matrix	2.16	0.98	22.67	20.30	52.73	1.17
2. Laves		3.74	5.19	5.14	67.05	18.89
3. Ni-rich precipitate		2.56	10.01	8.64	64.44	14.35
4. δ-Ni₃Nb	1.59	1.15	21.57	18.45	54.08	3.17

4.4.3 50h of exposure at 900°C

After 50 hours of exposure, the microstructure of the AM specimen and its composition are seen in Figure 44 and Table 23. The AM specimen formed a thin, oxide layer on its surface (region A), with thickness of about 2 μ m. EDS analysis yielded a composition that is near an atomic proportion of 2:3 for Cr:O; this layer is therefore identified as Cr₂O₃. This

chromia oxide layer A situates above a fine sublayer that is rich in Nb (region B), comparing to other layers. It is not clear if the layer B is oxide (Nb_2O_5) or intermetallic compound (Ni_3Nb) as EDS tends to gather information (particularly oxygen from layer A) from the surrounding area. There is also an occasional presence of NiO rich pegs (region C).

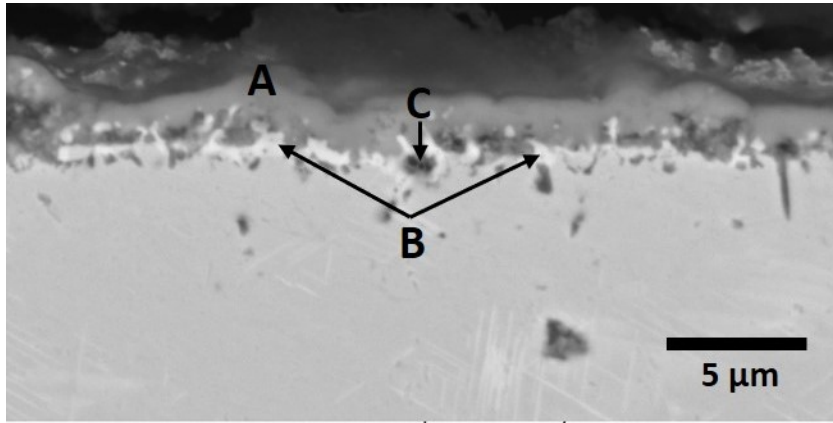


Figure 44. Oxide layers on AM Inconel 718 after 50h at 900°C

Table 23. Composition of AM Inconel 718 after 50h at 900°C

Element	Atomic %			Weight %		
	A	B	C	A	B	C
O K	69.23	34.18	29.85	41.03	11.64	10.43
Al K	0.53	1.41	5.67	0.53	0.81	3.34
Ti K	0.51	1.26	3.97	0.90	1.29	4.15
Cr K	28.48	7.32	8.46	54.85	8.11	9.60
Fe K	0.28	4.10	7.41	0.59	4.88	9.04
Ni K	0.97	39.90	36.29	2.11	49.89	46.52
Nb K		11.82	8.34		23.38	16.92

The baseline wrought Inconel 718 specimen presents a thicker chromia layer (region A in Figure 45 and compositions shown in Table 24) compared to the AM specimen. This layer

measures about 5 μm . Below this layer, there is also a Nb rich layer (B) but less regular than that seen on the AM specimens. There are very little Ni-rich precipitates (regions C) as compared to the AM specimen. These phases (B and C) are bigger in size than that seen in AM specimens.

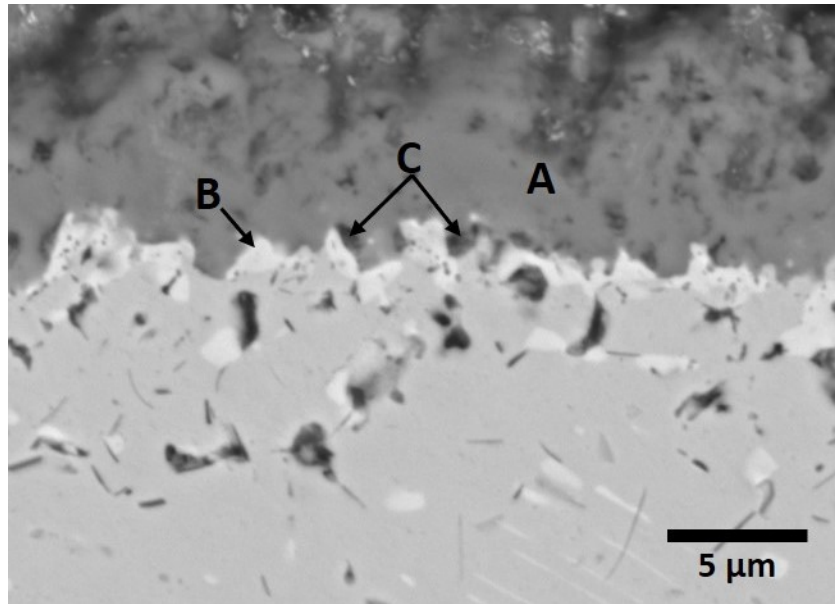


Figure 45. Oxide layers on the baseline wrought Inconel 718 after 50h at 900°C

Table 24. Composition of baseline wrought Inconel 718 after 50h at 900°C

Element	Atomic %			Weight %		
	A	B	C	A	B	C
O K	58.26	12.24	29.79	29.90	3.38	10.93
Al K	1.09		4.98	0.94		3.08
Ti K	2.67	0.58	2.34	4.11	0.48	2.57
Cr K	33.06	5.07	18.57	55.14	4.55	22.15
Fe K	1.94	7.38	11.36	3.47	7.11	14.55
Ni K	2.23	59.83	30.03	4.21	60.60	40.45
Nb K	0.75	14.90	2.94	2.23	23.89	6.26

4.4.4 100h of exposure at 900°C

The AM Inconel 718 exposed for 100h formed a continuous and thin chromia oxide scale as shown in Figure 46. This oxide layer is thickened that formed after 50h and measures to about 4 μm (compared region A in Figure 46 vs region A in Figure 44). Again, it is of Cr_2O_3 in nature (see Table 25 for its composition). Region B, just below the Cr_2O_3 , is an inner layer composed of likely intermetallic phase composed of Ni and Nb (Ni_3Nb sublayer) (Table 25). Furthermore, Ni/Fe-rich pegs (region C) formed further into the substrate, suggesting extended internal oxidation taking place (region C).

The EDS results of region B are in good agreement with that reported by Delaunay [76] and Pang et al. [77] who have also shown that at different exposure temperature, 700°C and 900°C, respectively, there is a segregation of Nb towards surface and a Ni_3Nb -rich layer is formed. This layer could have played an important role in enhancing the oxidation resistance of Inconel 718 by acting as an intermetallic diffusion barrier [78].

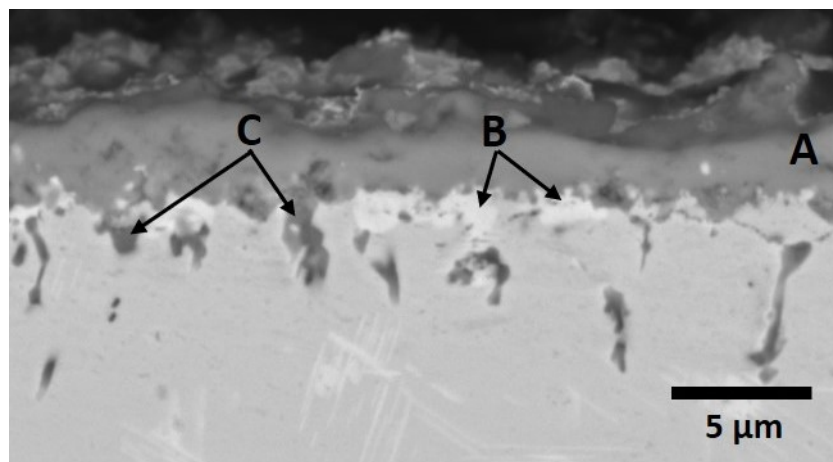


Figure 46. Oxide layers on AM Inconel 718 after 100h at 900°C

Table 25. Composition of AM Inconel 718 after 100h at 900°C

Element	Atomic %			Weight %		
	A	B	C	A	B	C
O K	63.42	9.90		33.82	2.84	
Al K	1.17	1.53		1.05	0.74	
Ti K	2.48	0.65	1.15	3.95	0.56	1.15
Cr K	25.55	7.15	11.81	44.28	6.68	11.81
Fe K	1.75	15.58	24.43	3.25	15.63	24.43
Ni K	3.36	57.32	60.83	6.58	60.43	60.83
Nb K	2.28	7.87	1.78	7.06	13.13	1.78

For the baseline wrought Inconel 718, the outer chromia oxide layer (region A in Figure 47) did not appear to grow in thickness; suggesting stabilized oxidation behaviours due possibly to the protective nature of previously formed Cr_2O_3 (compositions shown in Table 26). Below this oxide layer, there is again a Nb rich layer, similar to that found on the AM Inconel 718 specimens oxidized under the same condition. This presumed Ni_3Nb layer is now more continuous than that formed on specimens oxidized at 50h. It is however, surrounded fewer small Ni-rich precipitates (region C) and there is no obvious sign of internal oxidation as that seen on AM specimens oxidized under the same condition.

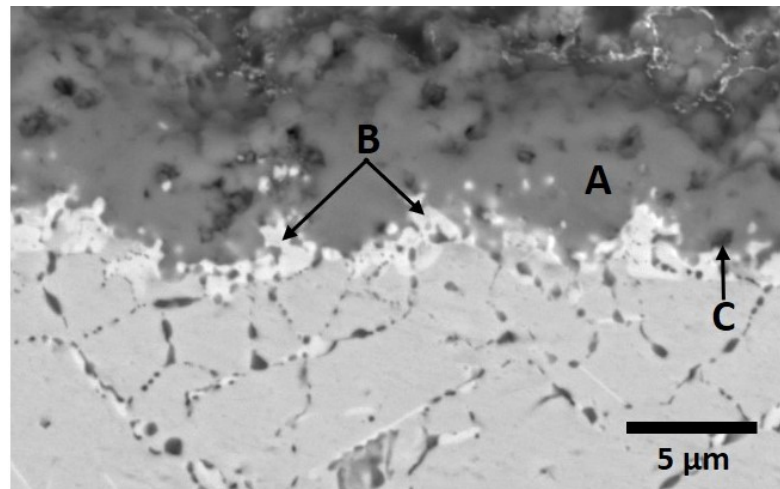


Figure 47. Oxide layers on the baseline wrought Inconel 718 after 100h at 900°C

Table 26. Composition of baseline wrought Inconel 718 after 100h at 900°C

Element	Atomic %			Weight %		
	A	B	C	A	B	C
O K	62.62	26.63	35.30	33.90	8.29	13.82
Al K	0.86		2.25	0.78		1.48
Ti K	2.64	2.32	13.56	4.28	2.16	15.89
Cr K	31.26	6.27	8.86	55.00	6.34	11.27
Fe K	0.53	3.72	12.03	1.01	4.04	16.43
Ni K	1.33	46.88	26.97	2.65	53.54	38.74
Nb K	0.76	14.18	1.04	2.38	25.63	2.37

4.4.5 200h exposure at 900°C

The chromia oxide layer formed on AM Inconel 718 after 200h of exposure has become uneven now (thickness ranges from 3 to 7 μm) and shows early indications of spallation (refer to region A in Figure 48). The early signs of spallation point to the onset of deterioration of the chromia oxide layer and a decline in mass would be expected with spallation after extended exposure. Pores are also observed in the substrate near the surface oxide. Porosity and voids have been shown to reduce ductility and increase stress ruptures in additive manufactured components [79]. The Nb containing layer is slightly thickened and but becomes more uneven (region B). Lastly, after 200h of exposure, it is believed that region C perhaps is composed of spinel $(\text{Cr,Al})(\text{Ni})_2\text{O}_4$ based on the presence of Ni, Cr, Al, and O (Table 27).

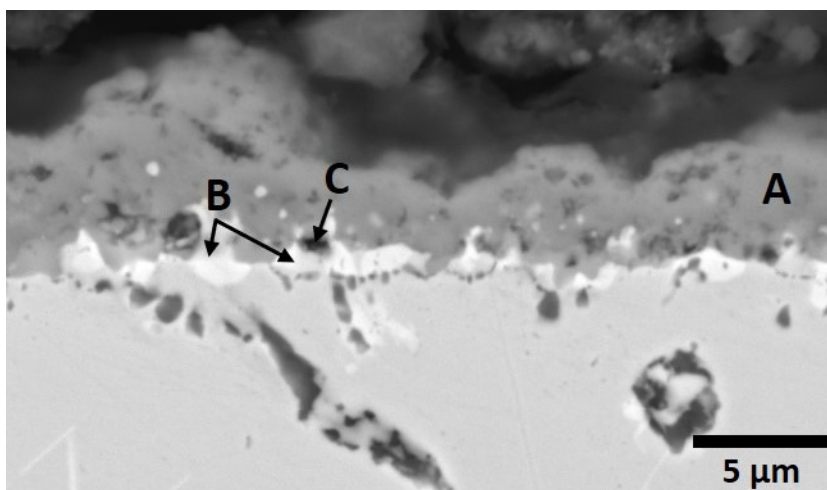


Figure 48. Oxide layers on AM Inconel 718 after 200h at 900°C

Table 27. Composition of AM Inconel 718 after 200h at 900°C

Element	Atomic %			Weight %		
	A	B	C	A	B	C
O K	62.64	12.62	45.39	34.13	3.43	18.06
Al K	0.56		2.10	0.52		1.41
Ti K	1.19	4.96	4.66	1.93	4.03	5.55
Cr K	33.79	4.53	15.41	59.84	4.00	19.93
Fe K	0.73	3.03	2.98	1.38	2.87	4.14
Ni K	1.10	55.81	20.16	2.20	55.63	29.44
Nb K		19.05	9.29		30.04	21.47

As for the baseline wrought Inconel 718 specimens, as shown in Figure 49, the outer chromia oxide layer seems to become somewhat uneven with peaks (10 μm) and valleys (6 μm) and porous. Located directly below the Cr₂O₃ layer, the Ni₃Nb sublayer (region B) continues to be present, although still uneven. Very few small Ni-rich precipitates are still present, in the vicinity of Nb-rich layer (region C did not seem to be spinel in nature, rather remains to be NiO as suggested by the elemental analysis results in Table 28).

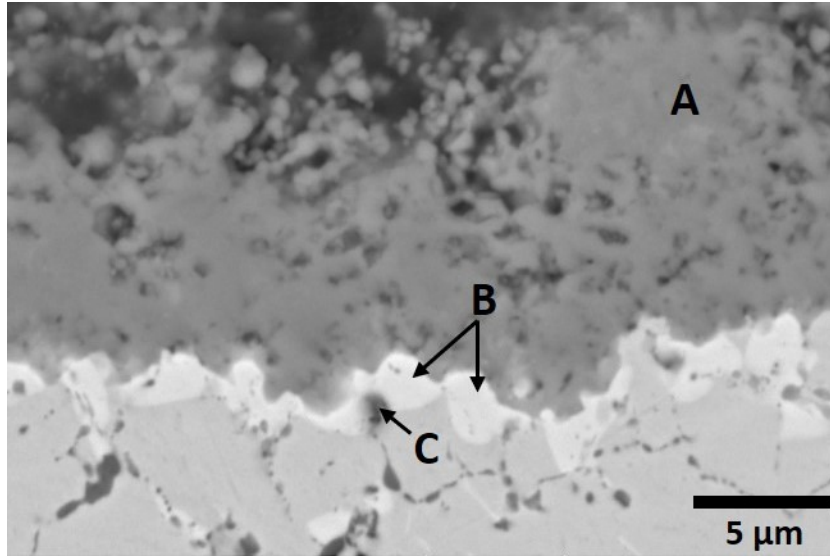


Figure 49. Oxide layers on the baseline wrought Inconel 718 after 200h at 900°C

Table 28. Composition of baseline wrought Inconel 718 after 200h at 900°C

Element	Atomic %			Weight %		
	A	B	C	A	B	C
O K	63.62	14.84	15.96	34.80	4.06	4.55
Al K			1.16			0.56
Ti K	0.57	1.46	0.87	0.93	1.20	0.74
Cr K	32.16	2.78	5.07	57.18	2.47	4.70
Fe K	2.41	3.46	7.57	4.61	3.30	7.54
Ni K	1.24	58.20	54.12	2.49	58.40	56.65
Nb K		19.26	15.24		30.57	25.25

Lastly, elemental mappings of the (a) AM and (b) baseline wrought Inconel 718 cross-sections were carried out and are presented in Figure 50. At 900°C, Inconel 718 formed primarily two layers, consisting of Cr₂O₃ for the outer layer, and an inner layer comprised of Ni₃Nb. Furthermore, it is apparent that the Cr-rich oxide layer is much thicker on the baseline wrought specimens while the distribution Nb (and Mo) in the sublayer is more continuous in the AM specimens. There are also obvious Al and Ti redistribution as a result of oxidation, mostly migrating towards outer surface.

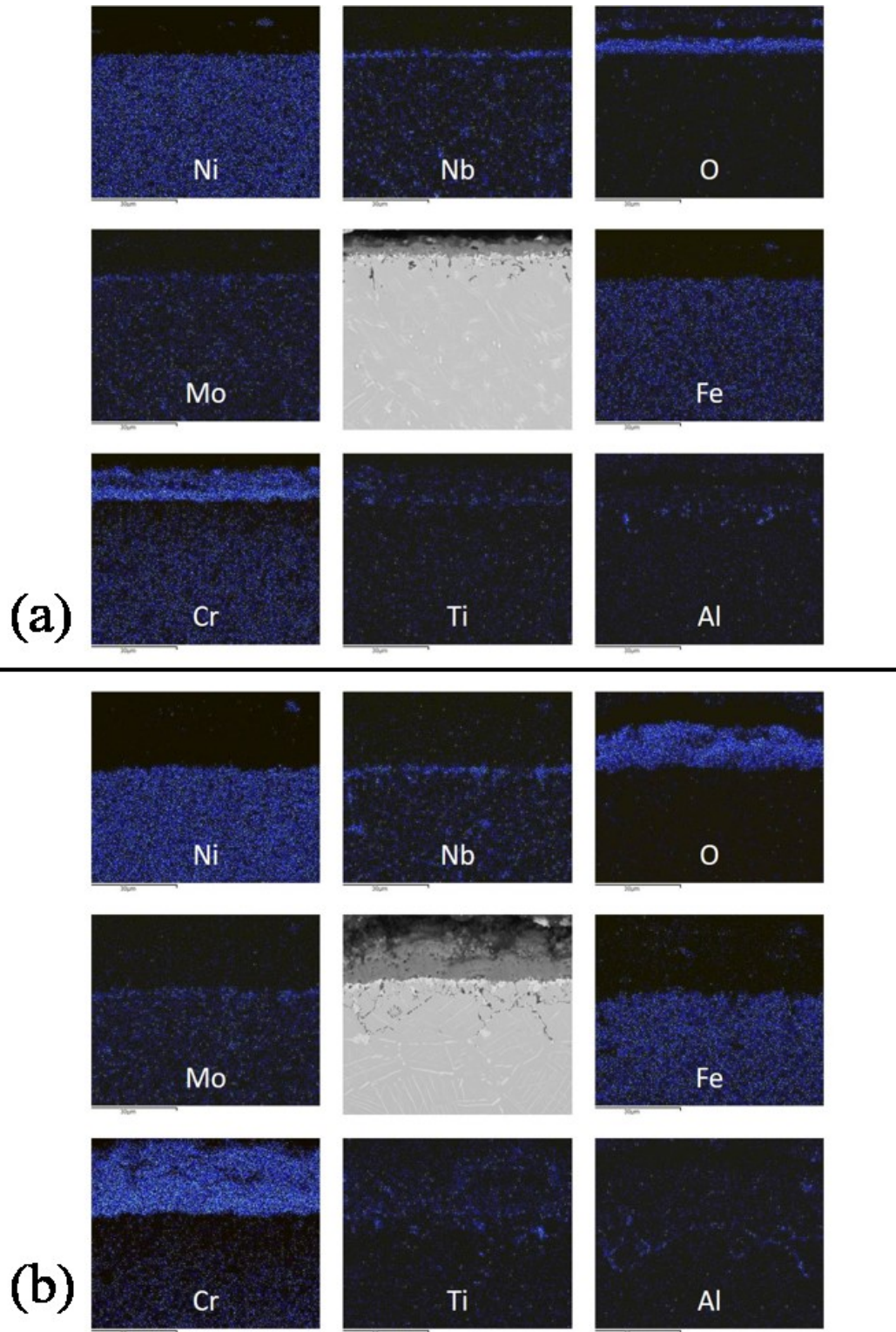


Figure 50. X-ray mapping of (a) AM and (b) Baseline wrought Inconel 718 after 200h at 900°C

In comparison to the 800°C specimens, the AM specimen presents more superficial Al-rich precipitates at 900°C. In the baseline wrought specimen, the Ti and Al rich regions are deeper into the matrix.

Chapter 5: Concluding Remarks

In this research, a plasma arc based additive manufacturing technique was used to produce large specimens for oxidation performance assessment. More specifically for this thesis, the focus was on comparing the oxidation behaviour of between the additively manufactured and baseline wrought Inconel 718 at two temperatures. Although based on the weight changes, the two alloys are on par in terms of weight gain, however, due to the difference in microstructure, several characteristics are different for the two alloys, namely the thickness of the oxide, the internal oxidation and also the changes in substrate microstructure as a function of temperature and exposure duration. Until the effect of process parameters on the microstructure (grain size, elemental segregation and secondary phases) is further understood, at this stage, it can only be concluded that the AM material produced has slightly inferior oxidation performance. This conclusion is based on the findings that a thicker and more stable chromia oxide layer, in addition to less internal oxidation, was found on the baseline wrought Inconel 718. A longer exposure time may perhaps yield equivalent oxidation resistance among the baseline wrought and the AM specimens as the onset of oxide spallation was observed after 200 hours at 900°C. A number of specific observations were also made during this study and are detailed as follows.

5.1 Effect of oxidation temperature

Formation of outer layer of chromia oxide are consistently found in both additively manufactured and baseline wrought Inconel 718. All specimens possess such protective layer above the matrix regardless of temperature or duration. It can be concluded, however,

that higher temperature yields thicker Cr_2O_3 layer, but their compactness and uniformity vary depending on the specimen type and heat treatment time. Also observed in this research is that, at both 800°C and 900°C , the AM specimen had a thinner chromia layer, and the baseline wrought specimen showed a uniform but thicker chromia layer until after 200 hours.

One other noticeable difference is that at the 800°C lower temperature, the Nb rich layer below the chromia is observed on baseline wrought specimens but not on AM specimens. At 900°C , both types of specimens have clear Nb-rich layer below the chromia. The Ni_3Nb sublayer is believed to have contributed to the consist oxide layer formed on the baseline wrought specimens. And the thickness of this Nb-rich sublayer increased with temperature and time. Additional research at lower and higher temperatures should be carried out to further study the correlation between oxidation resistance and the characteristics of the Nb-rich sublayer.

The increase in temperature from 800°C to 900°C also had an effect on the Ni-rich oxides formed in both specimens. At 900°C , this type of Ni-rich oxides is larger in size and could be found further extended into the matrix, particularly on the AM specimens. Given the fact that grain boundaries are not readily exhibited on the AM specimen (potentially a result of finer grain size from AM process), the relationship between the grain boundary and the Ni-rich oxide were not definable from this study.

5.2 Effect of exposure time

It is evident from this research that the formation of chromia oxide on both types of the specimens increases with time regardless of temperature. Based on the weight change and

the cross-sectional microstructure, the oxidation process appears to follow a parabolic rate of change. The chromia oxide layer formed increases initially in the early stage before becoming irregularly when spallation of the layer begins. In particular, the AM specimen showed signs of spallation after 200h at 900°C and the baseline wrought specimen after 400h at 800°C.

The protective Ni_3Nb sublayer is also independent on temperature, specially on the AM specimens in that there is hardly any Nb-rich sublayer formation after 100 h at 800°C. Irrespective of the temperature, both specimens exhibited increasing thickness of Nb-rich sublayers as time progressed.

The Ni-rich oxide tend to extend further into the substrate more with increased exposure time, primarily for the AM specimens, further suggesting the likelihood of internal oxidation on the AM Inconel 718 as exposure time increases.

5.3 Future Work

Based on the research obtained in this study, it is envisioned that further study will be required to study the additive manufacturing process parameters and post AM heat treatments in an effort to optimize the microstructure. Process parameter settings such as arc gap, material feed rate, laser power, travel speed, etc. could all impact material's microstructure hence properties.

Additional specimens should be exposed to the same temperature but for much longer times to understand the consumption and final depletion of Cr in this alloy. A final comparison of the two alloys can then be made when long-term oxidation tests are made available; the additional tests would provide a more adequate representation of a typical component's life

in a gas turbine. Tensile and fatigue tests are currently ongoing for the alloy used in this study and will be reported in the future.

With the availability of other AM techniques, a different AM technique can be used to produce similar specimens for comparability studies. Furthermore, homogenization heat treatment, in particular, should be examined thoroughly in an effort to optimize microstructure for both oxidation resistance and tensile properties.

References

- [1] M. Mani, K. W. Lyons, and S. K. Gupta, “Sustainability Characterization for Additive Manufacturing,” *J. Res. Natl. Inst. Stand. Technol.*, vol. 119, p. 419, Oct. 2014.
- [2] S. Ford and M. Despeisse, “Additive manufacturing and sustainability: an exploratory study of the advantages and challenges,” *Journal of Cleaner Production*, vol. 137. Elsevier Ltd, OXFORD, pp. 1573–1587, 2016.
- [3] A. Mouritz, *Introduction to Aerospace Materials*, 1st ed. Washington, DC: American Institute of Aeronautics and Astronautics, Inc., 2012.
- [4] A. S. Shaikh, “Development of a γ Precipitation Hardening Ni-Base Superalloy for Additive Manufacturing,” 2018.
- [5] A. F. El-Sayed, “Aircraft propulsion and gas turbine engines.” CRC Press, Taylor and Francis Group, London;New York;Boca Raton;, 2017.
- [6] R. C. Reed, *Superalloys - Fundamentals and Applications*. Cambridge University Press, 2006.
- [7] M. J. Donachie, S. Donachie, Donachie Mj, and Donachie Sj, *Superalloys : A Technical Guide*. Materials Park, UNITED STATES: A S M International, 2002.
- [8] K. Singh, “Advanced Materials for Land Based Gas Turbines,” *Trans. Indian Inst. Met.*, vol. 67, no. 5, pp. 601–615, 2014.
- [9] Y. N. Zhang, X. Cao, P. Wanjara, and M. Medraj, “Oxide films in laser additive manufactured Inconel 718,” *Acta Mater.*, vol. 61, no. 17, pp. 6562–6576, 2013.
- [10] M. Thomas, S. Murray, and D. Furrer, “Introducing New Materials into Aero Engines - Risks and Rewards, A User’s Perspective,” *Superalloy 718 and Derivatives - Proceedings of the 7th International Symposium on Superalloy 718 and Derivatives*. TMS (The Minerals, Metals & Materials Society), 2010.
- [11] R. Viswanathan and A. C. Dolbec, “Life Assessment Technology for Combustion Turbine Blades,” in *Volume 5: Manufacturing Materials and Metallurgy; Ceramics; Structures and Dynamics; Controls, Diagnostics and Instrumentation; Education; Process Industries*, 1986.
- [12] J. E. Watson, *Superalloys: Production, Properties and Applications*. Nova Science Publishers, 2011.
- [13] T. M. Pollock and S. Tin, “Nickel-Based Superalloys for Advanced Turbine Engines: Chemistry, Microstructure and Properties,” *Journal of Propulsion and Power*, vol. 22, no. 2. AMER INST AERONAUT ASTRONAUT, RESTON, pp. 361–374, 2006.
- [14] T. Pollock, “Alloy design for aircraft engines,” *Nat. Mater.*, vol. 15, pp. 809–815, Jul. 2016.
- [15] H.-J. Song, “Microstructural Evolution and Deformation Mechanisms in Nickel-Base SuperAlloys,” University of Cincinnati, University of Cincinnati, 2010.
- [16] N. S. Stoloff, W. C. Hagel, and C. T. 1923 Sims, *Superalloys II*. New York: Wiley, 1987.
- [17] A. Kracke, “Superalloys, The Most Successful Alloy System Of Modern Times - Past, Present And Future,” in *Superalloy 718 and Derivatives - Proceedings of the*

- 7th International Symposium on Superalloy 718 and Derivatives*, 2010, pp. 13–50.
- [18] J. N. DuPont 1964, J. C. Lippold, S. D. Kiser 1945, P. (Firm), and I. Books24x7, *Welding metallurgy and weldability of nickel-base alloys*, 1. Aufl. Hoboken, N.J: John Wiley and Sons, 2009.
- [19] H. Bor, C. Wei, H. T. Nguyen, A. Yeh, C. Kuo, and A. Engineering, “AGING EFFECTS ON THE γ' AND γ'' PRECIPITATES OF INCONEL 718,” in *Superalloy 718 and Derivatives - Proceedings of the 7th International Symposium on Superalloy 718 and Derivatives*, 2010, pp. 679–688.
- [20] Special Metals Corporation, “High-Performance Alloys for Resistance to Aqueous Corrosion,” 2000.
- [21] A. Jafari, A. Khorram, and S. M. A. Boutorabi, “Microstructure Evolution of MAR-M302 Superalloy During Heat Treatment at High Temperatures,” *Trans. Indian Inst. Met.*, vol. 71, no. 3, pp. 685–695, 2018.
- [22] J. F. Barker, “The Initial Years of Alloy 718: A GE Perspective,” in *Superalloys 718 Metallurgy and Applications (1989)*, 1989, pp. 269–277.
- [23] D. Zhao, S. Zhang, and C. R. C. Press, *Aerospace materials handbook*. Boca Raton, Fla: CRC Press, 2013.
- [24] D. G. Leo Prakash, M. J. Walsh, D. Maclachlan, and A. M. Korsunsky, “Crack growth micro-mechanisms in the IN718 alloy under the combined influence of fatigue, creep and oxidation,” *Int. J. Fatigue*, vol. 31, no. 11–12, pp. 1966–1977, 2009.
- [25] S. Sui, J. Chen, E. Fan, H. Yang, X. Lin, and W. Huang, “The influence of Laves phases on the high-cycle fatigue behavior of laser additive manufactured Inconel 718,” *Mater. Sci. Eng. A*, vol. 695, no. September 2016, pp. 6–13, 2017.
- [26] J. Cao, J. Zhang, R. Chen, Y. Ye, and Y. Hua, “High temperature oxidation behavior of Ni-based superalloy GH202,” *Mater. Charact.*, vol. 118, no. Complete, pp. 122–128, 2016.
- [27] C. Silva, M. Song, K. Leonard, M. Wang, G. Was, and J. Busby, “Characterization of alloy 718 subjected to different thermomechanical treatments,” *Mater. Sci. Eng. A*, vol. 691, pp. 195–202, Apr. 2017.
- [28] J. Strößner, M. Terock, and U. Glatzel, “Mechanical and Microstructural Investigation of Nickel-Based Superalloy IN718 Manufactured by Selective Laser Melting (SLM),” *Adv. Eng. Mater.*, vol. 17, no. 8, pp. 1099–1105, 2015.
- [29] D. Bourell *et al.*, “Materials for additive manufacturing,” *CIRP Ann. - Manuf. Technol.*, 2017.
- [30] M. Bogers, R. Hadar, and A. Bilberg, “Additive manufacturing for consumer-centric business models: Implications for supply chains in consumer goods manufacturing,” *Technol. Forecast. Soc. Chang.*, vol. 102, pp. 225–239, 2016.
- [31] Wholers Associate, “Annual World Wide Progress Report,” 2016.
- [32] T. DebRoy *et al.*, “Additive manufacturing of metallic components – Process, structure and properties,” *Progress in Materials Science*, vol. 92, 2018.
- [33] A. Mitchell, U. Lafont, M. Hołyńska, and C. Semprinoschnig, “Additive manufacturing — A review of 4D printing and future applications,” *Addit. Manuf.*, vol. 24, no. April, pp. 606–626, Dec. 2018.
- [34] I. Gibson and D. Rosen, *Additive Manufacturing Technologies*, Second. 2015.
- [35] ASTM International, “Standard Terminology for Additive Manufacturing – General

- Principles - Terminology,” vol. i, pp. 1–9, 2015.
- [36] W. E. Frazier, “Metal Additive Manufacturing: A Review,” *J. Mater. Eng. Perform.*, vol. 23, no. 6, pp. 1917–1928, Jun. 2014.
- [37] N. Tepylo, X. Huang, and P. Patnaik, “Review of AM for Aerospace and Defense Applications,” *Adv. Mater.*, 2019.
- [38] L. E. Murr and W. L. Johnson, “3D metal droplet printing development and advanced materials additive manufacturing,” *Journal of Materials Research and Technology*, vol. 6, no. 1. Elsevier Editora Ltda, AMSTERDAM, pp. 77–89, 2017.
- [39] J. J. Lewandowski and M. Seifi, “Metal Additive Manufacturing: A Review of Mechanical Properties,” *Annu. Rev. Mater. Res.*, vol. 46, no. 1, pp. 151–186, Jul. 2016.
- [40] D. Sun *et al.*, “Selective laser melting of titanium parts: Influence of laser process parameters on macro- and microstructures and tensile property,” *Powder Technol.*, vol. 342, pp. 371–379, 2019.
- [41] T. M. Mower and M. J. Long, “Mechanical behavior of additive manufactured, powder-bed laser-fused materials,” *Materials Science & Engineering A*, vol. 651. Elsevier B.V, LAUSANNE, pp. 198–213, 2016.
- [42] V. A. Popovich, E. V Borisov, A. A. Popovich, V. S. Sufiiarov, D. V Masaylo, and L. Alzina, “Impact of heat treatment on mechanical behaviour of Inconel 718 processed with tailored microstructure by selective laser melting,” *Mater. Des.*, vol. 131, pp. 12–22, 2017.
- [43] T. Raza, J. Andersson, and L.-E. Svensson, “Microstructure of Selective Laser Melted Alloy 718 in As-Manufactured and Post Heat Treated Condition,” *Procedia Manuf.*, vol. 25, pp. 450–458, 2018.
- [44] E. A. Alberti, B. M. P. Bueno, and A. S. C. M. D’Oliveira, “Additive manufacturing using plasma transferred arc,” *Int. J. Adv. Manuf. Technol.*, vol. 83, no. 9, pp. 1861–1871, 2016.
- [45] P. Bhargava *et al.*, “Tandem rapid manufacturing of Inconel-625 using laser assisted and plasma transferred arc depositions,” *Adv. Manuf.*, vol. 1, no. 4, pp. 305–313, 2013.
- [46] S. Jhavar, N. K. Jain, and C. P. Paul, “Development of micro-plasma transferred arc (μ -PTA) wire deposition process for additive layer manufacturing applications,” *J. Mater. Process. Tech.*, vol. 214, no. 5, pp. 1102–1110, 2014.
- [47] F. Martina, J. Mehnen, S. W. Williams, P. Colegrove, and F. Wang, “Investigation of the benefits of plasma deposition for the additive layer manufacture of Ti–6Al–4V,” *Journal of Materials Processing Tech*, vol. 212, no. 6. Elsevier B.V, LAUSANNE, pp. 1377–1386, 2012.
- [48] S. Jhavar, C. P. Paul, and N. K. Jain, “Micro-Plasma Transferred Arc Additive Manufacturing for Die and Mold Surface Remanufacturing,” *JOM*, vol. 68, no. 7, pp. 1801–1809, Jul. 2016.
- [49] R. Singh and M. B. Venkataraman, “High Temperature Corrosion and Oxidation of Metals,” *Metals*, vol. 9, no. 9. MDPI AG, p. 942, 2019.
- [50] X. Huang, “Oxidation.” p. 9.
- [51] S. Samal, “High-Temperature Oxidation of Metals,” in *High Temperature Corrosion*, Rijeka: InTech, 2016, p. Ch. 6.
- [52] G. Y. Lai and I. Books24x7, “High-temperature corrosion and materials applications

- .” ASM International , Materials Park, Ohio , 2007.
- [53] P. Marcus, “Corrosion mechanisms in theory and practice,” vol. 26;26.; CRC Press, Boca Raton, 2012.
- [54] S.-J. Park, S.-M. Seo, Y.-S. Yoo, H.-W. Jeong, and H. Jang, “Effects of Al and Ta on the high temperature oxidation of Ni-based superalloys,” *Corros. Sci.*, vol. 90, no. Complete, pp. 305–312, 2015.
- [55] T. Sanviemvongsak, D. Monceau, and B. Macquaire, “High temperature oxidation of IN 718 manufactured by laser beam melting and electron beam melting: Effect of surface topography,” *Corros. Sci.*, vol. 141, pp. 127–145, 2018.
- [56] C. Juillet, A. Oudriss, J. Balmain, X. Feaugas, and F. Pedraza, “Characterization and oxidation resistance of additive manufactured and forged IN718 Ni-based superalloys,” *Corros. Sci.*, vol. 142, pp. 266–276, 2018.
- [57] G. H. Cao *et al.*, “Investigations of γ' , γ'' and δ precipitates in heat-treated Inconel 718 alloy fabricated by selective laser melting,” *Mater. Charact.*, vol. 136, pp. 398–406, Feb. 2018.
- [58] H. T. Mallikarjuna, N. L. Richards, and W. F. Caley, “Isothermal Oxidation Comparison of Three Ni-Based Superalloys,” *J. Mater. Eng. Perform.*, vol. 26, no. 5, pp. 2014–2023, 2017.
- [59] M. Calandri *et al.*, “Solution Treatment Study of Inconel 718 Produced by SLM Additive Technique in View of the Oxidation Resistance ,” *Advanced Engineering Materials* , vol. 20, no. 11. WILEY-V C H VERLAG GMBH , WEINHEIM , pp. 1800351-n/a, 2018.
- [60] G. A. Greene and C. C. Finfrock, “Oxidation of Inconel 718 in Air t High Temperatures,” *Oxid. Met.*, vol. 55, p. 505, 2001.
- [61] Q. Jia and D. Gu, “Selective laser melting additive manufacturing of Inconel 718 superalloy parts : Densification , microstructure and properties,” *J. Alloys Compd.*, vol. 585, pp. 713–721, 2014.
- [62] Z. Wang, K. Guan, M. Gao, X. Li, X. Chen, and X. Zeng, “The microstructure and mechanical properties of deposited-IN718 by selective laser melting,” *J. Alloys Compd.*, vol. 513, pp. 518–523, 2012.
- [63] J. F. Radavich, “The Physical Metallurgy of Cast and Wrought Alloy 718,” in *Superalloys 718 Metallurgy and Applications (1989)*, 2004, pp. 229–240.
- [64] J. Gordine, “Some problems ins welding Inconel 718,” *Weld. J.*, no. 50, pp. 480–484, 1971.
- [65] P. C. Collins, D. A. Brice, P. Samimi, I. Ghamarian, and H. L. Fraser, “Microstructural Control of Additively Manufactured Metallic Materials ,” *Annual Review of Materials Research* , vol. 46, no. 1. Annual Reviews , PALO ALTO , pp. 63–91, 2016.
- [66] G. L. Knapp, N. Raghavan, A. Plotkowski, and T. DebRoy, “Experiments and simulations on solidification microstructure for Inconel 718 in powder bed fusion electron beam additive manufacturing,” *Addit. Manuf.*, vol. 25, pp. 511–521, 2019.
- [67] L. Rickenbacher, T. Etter, S. Hövel, and K. Wegener, “High temperature material properties of IN738LC processed by selective laser melting (SLM) technology ,” *Rapid Prototyping Journal* , vol. 19, no. 4. Emerald Group Publishing Limited , BINGLEY , pp. 282–290, 2013.
- [68] G. A. Greene and C. C. Finfrock, “Oxidation of Inconel 718 in Air at High

- Temperatures,” vol. 55, 2001.
- [69] J. T. Tharappel and J. Babu, “Welding processes for Inconel 718- A brief review ,” *IOP Conference Series: Materials Science and Engineering* , vol. 330, no. 1. p. 12082, 2018.
- [70] S. G. K. Manikandan, D. Sivakumar, and M. Kamaraj, “Physical metallurgy of alloy 718,” in *Welding the Inconel 718 Superalloy*, S. G. K. Manikandan, D. Sivakumar, and M. B. T.-W. the I. 718 S. Kamaraj, Eds. Elsevier, 2019, pp. 1–19.
- [71] E. Akca and A. Gürsel, “A Review on Superalloys and IN718 Nickel-Based INCONEL Superalloy ,” *Periodicals of Engineering and Natural Sciences (PEN)* , vol. 3, no. 1. 2015.
- [72] A. Devaux *et al.*, “Gamma double prime precipitation kinetic in Alloy 718,” *Mater. Sci. Eng. A*, vol. 486, no. 1, pp. 117–122, 2008.
- [73] A. Mitchell, “PRIMARY CARBIDES IN ALLOY 718,” in *Superalloy 718 and Derivatives - Proceedings of the 7th International Symposium on Superalloy 718 and Derivatives*, 2010, pp. 161–167.
- [74] B. Farber *et al.*, “Correlation of mechanical properties to microstructure in Inconel 718 fabricated by Direct Metal Laser Sintering,” *Mater. Sci. Eng. A*, vol. 712, pp. 539–547, 2018.
- [75] W. M. Tucho, P. Cuvillier, A. Sjolyst-kverneland, and V. Hansen, “Materials Science & Engineering A Microstructure and hardness studies of Inconel 718 manufactured by selective laser melting before and after solution heat treatment,” *Mater. Sci. Eng. A*, vol. 689, no. December 2016, pp. 220–232, 2017.
- [76] F. Delaunay, C. Berthier, M. Lenglet, and J.-M. Lameille, “SEM-EDS and XPS studies of the high temperature oxidation behaviour of Inconel 718,” *Microchim. Acta*, vol. 132, p. 337, 2000.
- [77] X. J. Pang, D. J. Dwyer, M. Gao, P. Valerio, and R. P. Wei, “Surface enrichment and grain boundary segregation of niobium in inconel 718 single- and polycrystals,” *Scr. Metall. Mater.*, vol. 31, no. 3, pp. 345–350, Aug. 1994.
- [78] K. Al-hatab, M. Al-bukhaiti, U. Krupp, and M. Kantehm, “Cyclic Oxidation Behavior of IN 718 Superalloy in Air at High Temperatures,” *Oxid. Met.*, vol. 75, no. 3–4, pp. 209–228, 2011.
- [79] X. Zhao, J. Chen, X. Lin, and W. Huang, “Study on microstructure and mechanical properties of laser rapid forming Inconel 718,” *Mater. Sci. Eng. A*, vol. 478, no. 1, pp. 119–124, 2008.